

# Theory of Berry Singularity Markers: Diagnosing Topological Phase Transitions via Lock-In Tomography

Panagiotis Kotetes\*

*CAS Key Laboratory of Theoretical Physics, Institute of Theoretical Physics,  
Chinese Academy of Sciences, Beijing 100190, China*

This work brings forward an alternative experimental approach to infer the topological character of phase transitions in insulators. This method relies on subjecting the target system to a set of external fields, each of which consists of two parts, i.e., a weak spatiotemporally slowly-varying component on top of a constant offset. The fields are chosen in such a way, so that they respectively induce slow variations in the wave vector describing the bulk band structure, as well as a parameter which allows tuning the bulk gap. Such a process maps the Berry singularities of the base space to a synthetic space spanned by the parameters related to the external fields. By measuring the response of the system to the weak part of the perturbations, when these are additionally chosen to form spacetime textures, one can construct a quantity that is here-termed Berry singularity marker (BSM). The BSM enables the Berry singularity detection as it becomes nonzero only in the close vicinity of a Berry singularity and is equal to its charge. The calculation of the BSM requires the measurement of the susceptibility tensor for the applied external fields. Near the Berry singularities, the BSM is dominated by a universal value, which is determined by the quantum metric tensor of the system. While in this work I restrict to 1D AIII insulators, the proposed approach is general. Notably, a key feature of the present method is that it can be implemented in a lock-in fashion, that is, one can “filter out” from the BSM any possible contribution from disorder by performing more measurements. Hence, the present construction paves the way for a disorder resilient diagnosis of topological phase transitions, that appears particularly relevant for disordered topological insulator and hybrid Majorana platforms, while it can be readily implemented using topo-electric circuits.

## I. INTRODUCTION

The discovery of new strategies to unambiguously detect the nontrivial character of topological materials and hybrid devices remains a pressing challenge in this timely research field. For instance, recent experiments [1–4] and theoretical studies [5–13] have highlighted the difficulties that are encountered when trying to distinguish Majorana zero modes (MZMs) from topologically-trivial Andreev bound states. While the latter originate from smooth confinement potentials or disorder [14–22], they may nonetheless become pinned near zero energy for an extended range in parameter space. Notably, such hurdles arise for the majority of topological systems, since the bulk nontrivial topology is typically inferred in experiments indirectly, that is, by probing the topologically-protected modes which emerge at boundaries where systems with different topological properties meet [23–27]. While this pursuit is certainly justified by the desire to harness the exotic properties of the arising modes for cutting edge applications [28, 29], this strategy has unavoidably hindered the development of possible methods to detect the bulk topology directly, i.e., by employing bulk-only measurements without involving the topologically-protected modes.

Recently, however, a number of theoretical proposals have appeared advocating for alternative experimental ways to infer the bulk topological properties of the system

of interest. For instance, in connection to MZMs, it has been proposed to probe the nonlocal conductance [30–35], the shot noise [36–41], or the equilibrium spin-susceptibility [42]. The spin-orbital magnetic susceptibility has been also proposed as a bulk-topology detection means for topological insulators [43]. Another proposed experimental method that has attracted attention is to infer properties of the bulk topology by studying the bound states of the system [44–46] which are induced by impurities [47]. The last development that I wish to mention here concerns the mapping out of the quantum geometry [48–50] which holds information for the quantum critical and topological properties of the bulk system [51–57]. For an insulator, its “imaging” can be achieved by inducing interband transitions to the system [58–66]. Up to date, the quantum geometry appears to have been successfully measured in various solid-state devices [67–72].

In this Article, I propose an alternative experimental approach which aims at directly diagnosing the bulk topology of a system using bulk-only equilibrium or quasi-equilibrium measurements. The present method relies on the observation that a phase transition separating two topologically-distinct phases is also endowed with topologically-nontrivial properties itself. Such an aspect appears to have been missed in the abovementioned works. Specifically, the target of the here-proposed experimental protocol is to map out the topological properties of the Berry singularities which characterize the bulk Hamiltonian and mediate the various topological phase transitions. The read-out of the topological charges and locations of Berry singularities is achieved by suitable mappings to a synthetic space which is spanned by a

---

\* kotetes@itp.ac.cn

set of  $N$  experimentally-controllable quantities comprising the vector  $\mathbf{F} = (F_1, F_2, \dots, F_N)$ .

In more detail, I suggest to experimentally carry out this new type of Berry-singularity tomography following a principle which bears close similarities to the one underlying the operation of the lock-in amplifier, cf Ref. 73. Thus, in analogy to the lock-in technique which enables the noise-free measurement of an electric signal by convoluting it with a sinusoidal reference signal, the present method promises the noise-free detection of Berry singularities by accordingly ‘‘convoluting’’ their Berry charge density with a reference field which possesses similar topological properties. As I argue, this convolution is achieved when the vector  $\mathbf{F}$  above possesses a suitable dependence on the spacetime coordinates  $\mathbf{X} = (\mathbf{r}, t)$ .

This work restricts to situations where  $\mathbf{F}(\mathbf{X})$  exhibits a slow spatial and/or temporal variation compared to the characteristic length/time scales governing the target system. Under this assumption, a semiclassical-type of approach becomes applicable, and one can theoretically predict the outcome of applying such fields by viewing the wave vector  $\mathbf{k}$  of the system as a variable which exhibits itself a correspondingly slow spatiotemporal variation. In fact, the external fields discussed here are chosen in such a way, so that they can induce the spatial and/or temporal variation of any of the components of  $\mathbf{k}$ , as well as the variation of an additional parameter  $M$  which tunes the size of the bulk energy gap and in turn controls the occurrence of topological phase transitions. A crucial aspect of the present method is how to choose the dependence of  $\mathbf{F}$  on  $\mathbf{X}$ . As it becomes clear later on, this is decided based on the expected topological properties of the target system. Nevertheless,  $\mathbf{F}$  obtains the general form  $\mathbf{F}(\mathbf{X}) = \mathbf{B} + \mathcal{B}(\mathbf{X})$  where  $\mathbf{B}$  defines a constant offset, while  $\mathcal{B}(\mathbf{X})$  gives rise to a topological texture characterized by the same kind of topological charge which is expected to classify the Berry singularities of the target bulk Hamiltonian. If little is known about the latter, then one has to proceed by testing various spacetime profiles in order to exhaust all the topological classes that are possible in the given spacetime dimensionality [23–27].

The engine of the here-proposed method relies on the construction of a quantity that I coin Berry singularity marker (BSM). The BSM enables the experimental diagnosis of the topological charges of the Berry singularities of the target Hamiltonian and their locations in the  $d$ -dimensional  $\mathbf{K} = (\mathbf{k}, M)$  space. The BSM is constructed as a suitable convolution of the reference fields  $(F_1, F_2, \dots, F_d)$ , and their experimentally measurable conjugate fields  $(P_1, P_2, \dots, P_d)$ . In the microcanonical statistical ensemble, the conjugate fields are defined as  $P_n(\mathbf{X}) = -\partial E / \partial F_n(\mathbf{X})$ , where  $E$  denotes the energy of the system and  $n = 1, 2, 3, \dots, d$ . As I detail in the remainder, the BSM tends by construction to a universal/topological value when  $\mathbf{B}$  is such, so that the system approaches a topological phase transition. At the same time, the value of  $\mathbf{B}$  required to observe the quantization of the BSM, also holds information regarding the

location of the Berry singularities in  $\mathbf{K}$  space. Thus, the BSM provides a measure for the distance away from the locations of the various Berry singularities and for this reason, it is naturally related to the so-called quantum or Fubini-Study metric [48] constructed using the Bloch band eigenvectors. Its value depends on the vector  $\mathbf{B}$  and the modulus  $\mathcal{B}(\mathbf{X}) = |\mathcal{B}(\mathbf{X})|$ . The latter variable quantifies the resolution of the experimental probe employed to perform the tomography proposed here. With no loss of generality, I assume that  $\mathcal{B}(\mathbf{X})$  is tailorable in experiments and is given by an  $\mathbf{X}$ -independent value which is from now on denoted  $\mathcal{B}$ .

Under the above conditions, the BSM construction which I present in the upcoming analysis guarantees that the BSM becomes equal to a topological invariant when:

$$\lim_{\mathcal{B} \rightarrow 0} \text{BSM}(\mathbf{B}_s, \mathcal{B}) = Q_s, \quad (1)$$

where  $Q_s$  defines the total topological charge of the Berry monopoles which mediate the topological phase transition across  $M = M_s$ , and  $\mathbf{B}_s$  is the value of  $\mathbf{B}$  which is required for tuning the system at the  $s$ -th phase transition. For a system lacking unitary symmetries, which is actually a prerequisite in the frame of the fundamental topological classification of insulators [23–27],  $Q_s$  stems from a single Berry singularity. In contrast, for a system with additional unitary symmetries, the contributions of symmetry-related Berry singularities are not independent and, thus, one can in principle disentangle the individual contribution of each one of the singularities.

In the following, I concretely exemplify how to construct the BSM for a representative AIII class topological insulator, which shares the same topological phenomenology with the Su-Schrieffer-Heeger (SSH) model [74]. Specifically, I examine the topological properties of this system in the presence of suitable external fields  $\mathbf{F}$ , demonstrate how the here-proposed experimental approach allows the detection of the underlying Berry singularities, and how the experimental measurements can be rendered quite insensitive to the presence of disorder.

The remainder is organized as follows. Section II describes the model Hamiltonian of the AIII topological insulator that I employ to demonstrate the here-proposed method. In Sec. III I discuss the coupling of the electrons to the external background fields and the synthetic-space mapping of the Berry singularities that these achieve. Sections IV and V focus on the response of the insulator to these external fields. They respectively discuss the properties of the conjugate fields and the generalized susceptibilities. Section VI contains the construction of the BSM, while Sec. VII reveals the link between the BSM and the quantum metric tensor that characterizes the valence band. The next two sections, i.e., Secs. VIII and IX focus on the implementation of the BSM using synthetic textures. Section X contains an analysis of the effects of random disorder on the BSM, and shows how the BSM can be shielded against noise by employing the lock-in principle. Section XI provides a summary and an

outlook. Finally, App. A discusses alternative possibilities regarding the coupling to the external fields, and App. B presents additional numerical calculations of the BSM in the presence of disorder.

## II. MODEL HAMILTONIAN

The approach proposed in this manuscript is demonstrated for the variant of the SSH model which is defined in terms of the single-particle Bloch Hamiltonian  $\hat{H}(\mathbf{K}) = \mathbf{d}(\mathbf{K}) \cdot \boldsymbol{\tau}$ , with the ‘‘isospin’’ vector:

$$\mathbf{d}(\mathbf{K}) = (\sin(k - k_0), 1 - \cos k + M, 0). \quad (2)$$

The wavenumber  $k$ , as well as the offset  $k_0$ , are defined in the Brillouin zone (BZ)  $[-\pi, \pi)$ . To represent the above  $2 \times 2$  matrix Hamiltonian I employ the ‘‘isospin’’  $\tau_{1,2,3}$  Pauli matrices and the respective unit matrix  $\mathbb{1}_\tau$ . While the precise nature of the  $\tau$  degree of freedom is irrelevant for the general idea behind the approach I present, this work is yet restricted to strictly non-superconducting systems. The above Hamiltonian possesses a chiral symmetry effected by  $\Pi = \tau_3$ , which establishes AIII as the ensuing symmetry class for the topological insulator. For convenience, I set  $k_0 = 0$  in the remainder, with the only exception to be Sec. X, where I discuss the effects of disorder sourced by randomly fluctuating  $k_0$  and  $M$ . Note that setting  $k_0 = 0$  gives rise to a charge-conjugation symmetry, which is generated by the complex conjugation operator  $\mathcal{K}$ . This additional symmetry modifies the symmetry class according to AIII  $\rightarrow$  BDI. Nevertheless, this change is insignificant for the results obtained in the upcoming analysis. Once again, I emphasize that the discussion of the lock-in tomography and its resilience against disorder are to be considered in the AIII model.

For the values  $M \neq \{-2, 0\}$ , the system described by Eq. (2) features a full gap in the bulk energy spectrum and resides in the topologically-nontrivial regime for  $M \in (-2, 0)$ , where it supports a single fractional zero-energy mode (FZM) at each edge of the system [75]. The characteristic feature of these FZMs is that they possess a fixed chirality  $\pm 1$ , i.e., the FZM eigenvectors are eigenstates of  $\Pi$ . Even more, FZMs on opposite edges see opposite chiralities. Hence, the fractionalization in the present case refers to the halving of the chirality degrees of freedom experienced by the zero-energy modes.

The topological properties and the absence/emergence of FZMs in the insulating phases occurring in the three parameter-value regimes  $M \in (-\infty, -2)$ ,  $(-2, 0)$ ,  $(0, \infty)$  are confirmed by evaluating the winding number [24]:

$$w = \int_{\text{BZ}} \frac{dk}{2\pi} \sum_{n,m} \varepsilon_{nm} \hat{d}_n(\mathbf{K}) \frac{\partial \hat{d}_m(\mathbf{K})}{\partial k} \quad (3)$$

where  $\varepsilon_{nm}$  denotes the antisymmetric Levi-Civita symbol with  $n, m = 1, 2$ , while  $\hat{\mathbf{d}}(\mathbf{K}) = \mathbf{d}(\mathbf{K})/|\mathbf{d}(\mathbf{K})|$  corresponds to the unit vector of  $\mathbf{d}(\mathbf{K})$ . One notes that the

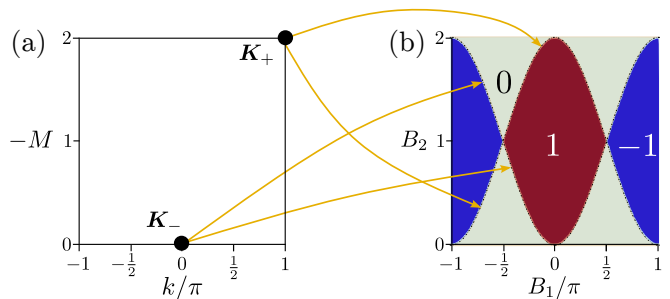


FIG. 1. Panel (a) depicts the two Berry singularities obtained from Eq. (2) in  $\mathbf{K} = (k, M)$  space for  $k_0 = 0$ . These carry topological charge  $\pm 1$  and are located at  $\mathbf{K}_+ = (\pi, -2)$  and  $\mathbf{K}_- = (0, 0)$ , respectively. (b) Topological phase diagram of model in Eq. (8) in the synthetic  $\mathbf{B}$  space. The numbers shown correspond to the outcome of the winding number  $w$  for  $k_0 = M = 0$ . The Berry singularities are mapped from  $\mathbf{K}$  to  $\mathbf{B}$  space. Note that the mapping of the topological charges may differ up to an overall sign depending on the quadrant in synthetic space. The Berry vortices in  $\mathbf{K}$  space also map to the remaining parts of the lines obtained by  $B_1 \mapsto -B_1$ , which are not shown here.

difference of  $w$  across a bulk topological phase transition occurring at  $M = M_s$ , which is defined as:

$$\Delta w_s = w(M = M_s^+) - w(M = M_s^-) \quad (4)$$

yields the *total* topological charge  $Q_s$  of the Berry monopoles of  $\hat{H}(\mathbf{K})$  which are responsible for the transition. Note that, in the present case, the Berry singularities correspond to vortices in 2D  $\mathbf{K} = (k, M)$  space, which appear at the locations  $\mathbf{K}_s = \{(\pi, -2), (0, 0)\}$  with  $s = \pm$ . The two Berry vortices are depicted in Fig. 1(a).

The charge of each Berry vortex can be equivalently obtained by means of the line integral:

$$Q_s = - \oint_{\mathcal{C}_{\mathbf{K}_s}} \frac{d\mathbf{K}}{2\pi} \cdot \sum_{n,m} \varepsilon_{nm} \hat{d}_n(\mathbf{K}) \frac{\partial \hat{d}_m(\mathbf{K})}{\partial \mathbf{K}}, \quad (5)$$

where  $\mathcal{C}_{\mathbf{K}_s}$  is a loop which encircles the singularity located at  $\mathbf{K}_s$  and  $n, m = 1, 2$ . In fact, Eq. (4) originates from Eq. (5) after a particular path  $\mathcal{C}_{\mathbf{K}_s}$  has been chosen.

The topological charge can be alternatively expressed in terms of the Berry vector potential  $\mathbf{A}_\pm(\mathbf{K})$  of the Bloch eigenstates  $|\mathbf{u}_\pm(\mathbf{K})\rangle$  corresponding to the energy dispersions  $E_\pm(\mathbf{K}) = \pm|\mathbf{d}(\mathbf{K})|$ . In the present case, the Berry vector potential is the same for both bands and is defined as:

$$\mathbf{A}(\mathbf{K}) = i \langle \mathbf{u}_-(\mathbf{K}) | \partial_{\mathbf{K}} \mathbf{u}_-(\mathbf{K}) \rangle = -\frac{1}{2} \varepsilon_{nm} \hat{d}_n(\mathbf{K}) \frac{\partial \hat{d}_m(\mathbf{K})}{\partial \mathbf{K}} \quad (6)$$

which allows to rewrite  $Q_s$  in the compact form:

$$Q_s = \frac{1}{\pi} \oint_{\mathcal{C}_{\mathbf{K}_s}} d\mathbf{K} \cdot \mathbf{A}(\mathbf{K}). \quad (7)$$

From either one of the above equivalent definitions, one finds that the Berry vorticities across the two transitions at  $M_{\pm} = \{-2, 0\}$  are correspondingly  $Q_{\pm} = \{1, -1\}$ .

Being in a position to know the topological charges and locations of the Berry singularities allows us to reconstruct the entire topological phase diagram of the system, as long as the topological properties of the system are known for a single value of  $M$ . For convenience, this value can be associated with a well-known limiting topological behavior of the system. For instance, for the vector  $\mathbf{d}(\mathbf{K})$  considered in Eq. (2), the limits  $M \rightarrow \pm\infty$  lead to a topologically-trivial system, which is a piece of information that is typically accessible in experiments.

### III. BERRY-SINGULARITY MAPPING TO A SYNTHETIC SPACE

In this paragraph, I proceed by describing the coupling of the system to the external fields  $\mathbf{F}$ . Within the throughout-adopted semiclassical limit, I assume that these couple to the system through generating a spatiotemporal variation for  $\mathbf{K}$ , so that near the Berry singularities we have  $d\mathbf{K}/d\mathbf{X} \sim d\mathbf{F}/d\mathbf{X} = d\mathcal{B}/d\mathbf{X}$ . For the model of Eq. (2), I first consider the following concrete type of coupling:<sup>1</sup>

$$\mathbf{d}(\mathbf{K}, \mathbf{F}) = (\sin(k - k_0 - F_1), 1 - \cos k + M - F_2, 0), \quad (8)$$

which gives rise to the accordingly modified energy dispersions that I denote  $E_{\pm}[\mathbf{K}, \mathbf{F}(\mathbf{X})] = \pm|\mathbf{d}(\mathbf{K}, \mathbf{F})|$ .

Within the semiclassical picture adopted here, the presence of the fields allow us to map the Berry singularities from  $\mathbf{K}$  space to  $\mathbf{F}$  space. The Berry singularities appear at the two  $\mathbf{F}$ -dependent locations in  $\mathbf{K}$  space:

$$\begin{aligned} \mathbf{K}_+(\mathbf{F}) &= (\pi + F_1 + k_0, F_2 - \cos(F_1 + k_0) - 1), \\ \mathbf{K}_-(\mathbf{F}) &= (F_1 + k_0, F_2 + \cos(F_1 + k_0) - 1). \end{aligned} \quad (9)$$

After considering  $\mathcal{B} = 0$  for the moment, the above results imply that by solely restricting to  $\mathbf{B}$  space, the two Berry singularities appear respectively along the trajectories:

$$B_2 = 1 \pm \cos(B_1 + k_0) + M. \quad (10)$$

<sup>1</sup> Note that the above prescription for the coupling is not unique. In fact, App. A discusses an alternative coupling. Furthermore, extra caution should be paid on the choice of the coupling and the nature of the fields  $\mathbf{F}$  when discussing spatial textures for  $\mathbf{F}(\mathbf{X})$ . Specifically, one should avoid employing U(1) gauge fields for  $\mathbf{F}$  in this case. This is because the gauge freedom allows to remove static U(1) gauge fields from the Hamiltonian and absorb them into twisted boundary conditions. However, such “large” gauge transformations are not equivalent to the spatial textures that are assumed throughout this work.

These two Berry singularity branches are overlaid with dot-dashed lines on the topological phase diagram presented in Fig. 1(b). The latter is defined solely in  $\mathbf{B}$  space and is obtained under the assumption  $k_0 = M = \mathcal{B} = 0$ .

The above results imply that, by introducing the external fields, we are in a position to map out the topological phase diagram of the system, even without knowing the exact Hamiltonian of the system. While the importance of inferring the Hamiltonian is certainly indisputable, in actual experiments the priority is to be able to manipulate the properties of the system using the external parameters. Hence, from this point of view, mapping the Berry singularities onto the synthetic space spanned by the control fields is more important when it comes to potential applications. Evenmore, “transferring” the Berry singularities to a synthetic space has advantages, since there, the Berry singularities are present in an extended window and form lines, thus rendering this approach preferred for their study.

To this end, I stress that the role played by the synthetic space in this work and the purpose for its use, are clearly different than the ones of a number of recent studies regarding conventional [76–81] and topological [82–86] superconductors, which discuss topological phases and Berry singularities in a synthetic space. There, the topological properties are associated with a Hamiltonian which depends on the synthetic space coordinates. Here instead, the focus is on the parametric dependence of the conjugate fields, which constitute expectation values of the Hamiltonian of interest. The goal is to employ the external fields as a means to manipulate the response of the system and infer the topological properties of the underlying Hamiltonian.

### IV. RESPONSE TO THE EXTERNAL FIELDS

The above method of imprinting the Berry singularities onto a synthetic space allows for their identification through the study of the response of the system to these external fields. As announced earlier, I consider external fields which consist of two components, the offset  $\mathbf{B}$  and the spatio/temporal varying  $\mathcal{B}(\mathbf{X})$ . The role of  $\mathbf{B}$  is to control the topological properties of the system, and tune it near a topological phase transition, as it was demonstrated in the previous section. Being in a position to controllably approach a topological phase transition, at the same time allows us to tune the system near the location of a Berry singularity in synthetic space. On the other hand, the additional  $\mathcal{B}(\mathbf{X})$  component functions as a weak perturbation which is employed to assert the presence of the Berry singularity and, hence the topological character of the associated phase transition. The introduction of  $\mathcal{B}(\mathbf{X})$  also opens the door for a lock-in type of experimental detection of the Berry singularity charge. As I detail later on, this lock-in approach provides a route to filter out the effects of noise and disorder from the measurements.

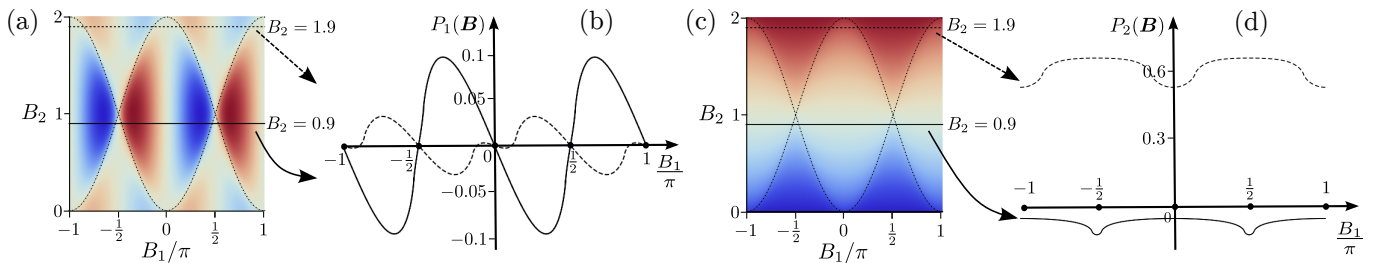


FIG. 2. Numerical evaluation of  $\mathbf{P}(\mathbf{B})$ , which is defined by setting  $\mathcal{B} = 0$  in  $\mathbf{P}(\mathbf{F})$ . Panels (a) and (c) depict a heat map of  $P_{1,2}(\mathbf{B})$  as functions of  $(B_1, B_2)$ . The latter are sampled in the most interesting parameter-value window, in which Berry singularity branches exist. In (a) and (c), the colorcoding varies continuously between deep red to deep blue (→), which one-to-one correspond to the maximum and minimum of the depicted function. In both panels, I have superimposed the contour plots  $B_2 \pm \cos B_1 = 1$  which yield the locations of the Berry singularities in the synthetic  $\mathbf{B}$  space for  $k_0 = M = 0$ , which are values that I considered for the calculations presented here. Panels (b) and (d) show the dependence of  $P_1(\mathbf{B})$  and  $P_2(\mathbf{B})$ , respectively, for two specific cuts of (a) and (c). These two cuts are for  $B_2 = 1.9$  and  $B_2 = 0.9$ .

The response of the system is encoded in the conjugate fields  $\mathbf{P}[\mathbf{F}(\mathbf{X})]$ . These are measured under fully/quasi-equilibrium conditions, since  $\mathbf{F}(\mathbf{X})$  is here restricted to vary adiabatically in time. In the zero-temperature limit of interest, these receive contributions only from the occupied band of the Hamiltonian defined by Eq. (8). The above conditions lead to the expression:

$$\begin{aligned} P_n[\mathbf{F}(\mathbf{X})] &= -\frac{\partial}{\partial F_n(\mathbf{X})} \int_{\text{BZ}} \frac{dk}{2\pi} E_-[\mathbf{K}, \mathbf{F}(\mathbf{X})] \\ &= \int_{\text{BZ}} \frac{dk}{2\pi} \hat{\mathbf{d}}(\mathbf{K}, \mathbf{F}(\mathbf{X})) \cdot \frac{\partial \mathbf{d}(\mathbf{K}, \mathbf{F}(\mathbf{X}))}{\partial F_n(\mathbf{X})}. \end{aligned} \quad (11)$$

To gain further insight regarding the properties of the system, I set  $\mathcal{B} = 0$  and calculate the conjugate fields as functions of  $B_{1,2}$ . For convenience, I assume  $k_0 = M = 0$ , and restrict to the regime  $B_1 \in [-\pi, \pi]$  and  $B_2 \in [0, 2]$ , where Berry singularities become accessible in the respective synthetic  $\mathbf{B}$  space. From the panels of Fig. 2, one observes that the vector  $\mathbf{P}(\mathbf{B})$  and the synthetic coordinates  $\mathbf{B}$ , present an analogy to  $\mathbf{d}(\mathbf{K})$  and  $\mathbf{K}$ , when it comes to their symmetry properties. Hence, based on the correspondence  $\mathbf{d}(\mathbf{K}) \mapsto \mathbf{P}(\mathbf{B})$ , one expects that similar to  $\mathbf{d}(\mathbf{K})$ , which can be employed to define a nonzero vorticity in  $\mathbf{K}$  space, the conjugate vector field  $\mathbf{P}(\mathbf{B})$  can be employed to define vorticity in  $\mathbf{B}$  space. However, such a construction is not possible since, in contrast to  $|\mathbf{d}(\mathbf{K}, \mathbf{B})|$ , the modulus  $|\mathbf{P}(\mathbf{B})|$  does not necessarily contain zeros, and if it does, these do not have to coincide with the zeros of  $|\mathbf{d}(\mathbf{K}, \mathbf{B})|$  when restricted to  $\mathbf{B}$  space. Nevertheless, the behaviour of  $\mathbf{P}(\mathbf{B})$  is significantly influenced by the presence of the Berry singularities in synthetic space, since the variations of  $\mathbf{P}(\mathbf{B})$  closely track the lines of the synthetic space Berry singularities given by Eq. (10). It is exactly this property which allows us to identify the presence of Berry singularities by extracting information about the variations of  $\mathbf{P}(\mathbf{B})$ .

## V. PERTURBATIONS ABOUT THE BERRY SINGULARITIES

As mentioned above, one cannot directly use the conjugate fields  $\mathbf{P}(\mathbf{B})$  or similarly  $\mathbf{P}(\mathbf{F})$  to construct a topological invariant which can be associated with the Berry singularities in synthetic  $\mathbf{F}$  space and, in turn, in  $\mathbf{K}$  space. Nonetheless, the conjugate fields still hold information regarding the position and the charge of the Berry singularities in the synthetic space. This information can be accessed by decomposing the field  $\mathbf{F}$  into the two contributions  $\mathbf{B}$  and  $\mathcal{B}$ , with the latter containing the slow spatiotemporal variations mentioned earlier.

The crucial observation here is that when  $\mathcal{B} \rightarrow 0$ , the response of the system can be retrieved by expanding the conjugate fields up to first order in  $\mathcal{B}$ . Such an expansion leads to the expression:

$$P_n[\mathbf{F}(\mathbf{X})] \approx P_n(\mathbf{B}) + \chi_{nm}(\mathbf{B}) \mathcal{B}_m(\mathbf{X}) \quad (12)$$

where I introduced the generalized susceptibilities:

$$\chi_{nm}(\mathbf{B}) = \left. \frac{\partial P_n(\mathbf{F})}{\partial F_m} \right|_{\mathcal{B}=0}, \quad (13)$$

which in the present case obtain the following form:

$$\begin{aligned} \chi_{nm}(\mathbf{B}) &= \int_{\text{BZ}} \frac{dk}{2\pi} \left[ \frac{\partial \hat{\mathbf{d}}(\mathbf{K}, \mathbf{B})}{\partial B_m} \cdot \frac{\partial \mathbf{d}(\mathbf{K}, \mathbf{B})}{\partial B_n} \right. \\ &\quad \left. + \hat{\mathbf{d}}(\mathbf{K}, \mathbf{B}) \cdot \frac{\partial^2 \mathbf{d}(\mathbf{K}, \mathbf{B})}{\partial B_m \partial B_n} \right]. \end{aligned} \quad (14)$$

From the above, one also obtains the equality relation  $\chi_{21}(\mathbf{B}) = \chi_{12}(\mathbf{B})$  for the off-diagonal tensor elements, since Eq. (14) is symmetric under the exchange  $1 \leftrightarrow 2$ .

In Fig. 3, I present the outcome for each one of the three susceptibility tensor elements  $\chi_{11,22,12}(\mathbf{B})$ . As assumed in the calculation concerning the conjugate fields, the values  $k_0 = M = 0$  are considered also here. One observes that the three susceptibilities  $\chi_{11,22,12}(\mathbf{B})$

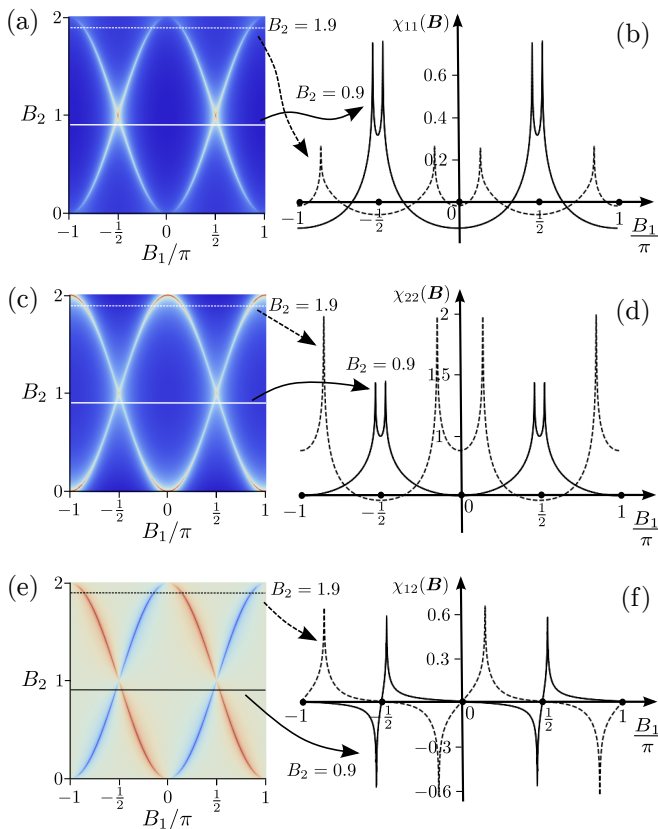


FIG. 3. Depiction of the numerically evaluated susceptibility tensor elements  $\chi_{11,22,12}(\mathbf{B})$ . Note that  $\chi_{21}(\mathbf{B}) = \chi_{12}(\mathbf{B})$ . Panels (a), (c) and (e) present heat maps of the susceptibilities as functions of  $(B_1, B_2)$ . The parameter window coincides with the one considered in Fig. 2. In a similar fashion to the latter, also here, the heat map’s colorcoding varies continuously between deep red to deep blue (■), which one-to-one correspond to the maximum and minimum of the depicted function. Panels (b), (d) and (f) show the dependence of  $\chi_{11,22,12}(\mathbf{B})$ , for two specific cuts of (a), (c) and (e), respectively. These two cuts are also here for  $B_2 = 1.9$  and  $B_2 = 0.9$ . In order to smoothen out the peaks appearing at the singularities, I introduced to the Hamiltonian an additional term  $d_3(\mathbf{K})\tau_3$  with a small nonzero component  $d_3(\mathbf{K}) = 2 \cdot 10^{-3}$ . This “trick” is employed in all calculations to follow, as long as these involve the evaluation of the susceptibility tensor elements. All the results are obtained for the values  $k_0 = M = 0$ .

become considerable mainly at the locations  $\mathbf{B}_\pm$  of the Berry singularities, which are given by  $(B_1, B_2) = (B_1, 1 \pm \cos B_1)$ . Hence, either susceptibility can be employed to identify the two Berry singularity branches. In addition, we observe that  $\chi_{11,22}(\mathbf{B})$  are positive in the vicinity of the Berry singularities. Instead,  $\chi_{12}(\mathbf{B})$  presents sign changes which reflect the symmetry properties of the system, and follows a distinctive pattern when it comes to the two Berry singularity branches. In particular, we find that the two branches are characterized by opposite  $\chi_{12}(\mathbf{B})$  which can be associated with the

sign of the topological charge of the Berry singularities at  $\mathbf{B}_+ = (0, 2)$  and  $\mathbf{B}_- = (0, 0)$ , which map one-to-one the two  $\mathbf{K}_\pm$  singularities in  $\mathbf{K}$  space, as shown in Fig. 1.

## VI. CONSTRUCTION OF THE BSM

The above conclusions regarding the response of the system are the ones that strongly motivate the introduction of the additional field  $\mathbf{B}$ . To make this transparent I study the properties of the following line integral:

$$I_s(\mathbf{B}) = - \sum_{n,m} \oint_{\mathcal{C}_{\mathbf{B}_s}} d\mathcal{B}_n \varepsilon_{nm} P_m(\mathbf{B}_s + \mathbf{B}). \quad (15)$$

The above construction is inspired by Eq. (7) and bears analogies to it. There, the line integral involves the Berry vector potential  $\mathbf{A}(\mathbf{K})$  for the occupied band. Here, one aims at defining a quantity which is analogous to  $\mathbf{A}(\mathbf{K})$ .

To achieve this goal, it is pivotal to investigate the behaviour of  $I_s$  for a sufficiently small  $\mathbf{B} = |\mathbf{B}(\mathbf{X})|$ , so that the system lies in the vicinity of the Berry singularity. In this event,  $I_s$  is approximately given by:

$$I_s(\mathbf{B}) \approx - \sum_{n,m} \varepsilon_{nm} \chi_{m\ell}(\mathbf{B}_s) \oint_{\mathcal{C}_{\mathbf{B}_s}} d\mathcal{B}_n \mathcal{B}_\ell, \quad (16)$$

since the contribution proportional to  $P_n(\mathbf{B}_s)$  drops out after integrating over the closed path  $\mathcal{C}_{\mathbf{B}_s}$ . It is straightforward to evaluate the line integral. By considering for instance a circular path  $\mathcal{C}_{\mathbf{B}_s}$ , which is defined through setting  $\mathbf{B} = \mathcal{B}(\cos \omega, \sin \omega)$  with  $\omega \in [0, 2\pi)$ , one obtains:

$$\oint_{\mathcal{C}_{\mathbf{B}_s}} d\mathcal{B}_n \mathcal{B}_\ell = \mathcal{B}^2 \int_0^{2\pi} d\omega \frac{d\mathcal{B}_n}{d\omega} \mathcal{B}_\ell = -\pi \mathcal{B}^2 \varepsilon_{n\ell}. \quad (17)$$

The above result implies that in the limit  $\mathbf{B} \rightarrow 0$ ,  $I_s$  tends to the value:

$$I_s(\mathbf{B} \rightarrow 0) \approx \pi \mathcal{B}^2 [\chi_{11}(\mathbf{B}_s) + \chi_{22}(\mathbf{B}_s)] \equiv \pi \mathcal{B}^2 \text{Tr}[\check{\chi}(\mathbf{B}_s)], \quad (18)$$

where I introduced the generalized susceptibility tensor denoted here  $\check{\chi}$ , along with the trace operation in the space spanned by its indices.

At this point I remind the reader that all the susceptibilities diverge at the Berry singularity branches, and in fact only at these. Therefore, since  $I_s(\mathbf{B})$  becomes substantial practically only near the  $s$ -th Berry singularity, it can supply us with a notion of a distance from this singularity. Indeed, as I discuss in the next section, this conclusion is further backed by the fact that  $I_s$  relates to the quantum metric tensor  $\check{g}$  which quantifies the distance between two quantum states. Note that the utility of  $\check{g}$  in asserting the occurrence of phase transition has already been emphasized in previous works [52–54]. From a practical point of view, here, one can simply “normalize”  $I_s(\mathbf{B})$  for a vector  $\mathbf{B}$  of an arbitrary strength  $\mathcal{B}$ , by

dividing it by  $I_s(\mathcal{B} \rightarrow 0)$ , in order to obtain a normalized distance from the Berry singularity and infer the location of the latter in synthetic space.

Despite the fact that  $I_s$  provides a measure of distance from Berry singularities, it nevertheless cannot provide information regarding the sign of the charge of the Berry singularities, since the sign of  $I_s$  is fixed. To tackle this problem, I introduce a quantity which plays an analogous role to the Berry vector potential and is defined as:

$$\mathcal{A}_n(\mathbf{B}, \mathcal{B}) = -\frac{\text{sgn}[\chi_{12}(\mathbf{B})]}{\text{Tr}(\tilde{\chi}_{\text{BS}})\mathcal{B}} \varepsilon_{nm} P_m(\mathbf{B} + \mathcal{B}), \quad (19)$$

where the sign of the susceptibility  $\chi_{12}(\mathbf{B})$  is introduced in order to provide the so-far missing piece of information regarding the sign of the charge of the Berry singularity. The quantity  $\text{Tr}(\tilde{\chi}_{\text{BS}})$  denotes the value of  $\text{Tr}(\tilde{\chi})$  evaluated at the location of the Berry singularity which is the closest to the synthetic space location  $\mathbf{B}$  of interest. Such an approach is employed for the numerical studies in Sec. IX. Notably, in case the trace of the susceptibility is fully determined by the quantum metric tensor  $\check{g}$ ,  $\text{Tr}(\tilde{\chi}_{\text{BS}})$  becomes a universal constant in almost the entire synthetic space. This holds when the diamagnetic contributions to the susceptibilities are either negligible or precisely zero, as I clarify in the next section.

Under the above conditions, and in analogy to the line integral in Eq. (16), I construct the BSM as follows:

$$\mathcal{Q}(\mathbf{B}, \mathcal{B}) = \frac{1}{\pi} \oint_{\mathcal{C}_{\mathbf{B}}} d\hat{\mathbf{B}} \cdot \mathcal{A}(\mathbf{B}, \mathcal{B}), \quad (20)$$

where  $\hat{\mathbf{B}} = \mathcal{B}/\mathcal{B}$  and  $\mathcal{C}_{\mathbf{B}}$  defines a closed path defined by  $\mathcal{B}$  centered at the location  $\mathbf{B}$ . Notably, the BSM tends to a quantized value for  $\mathcal{B} \rightarrow 0$ , that is:

$$\lim_{\mathcal{B} \rightarrow 0} \mathcal{Q}_s(\mathcal{B}) = \text{sgn}[\chi_{12}(\mathbf{B}_s)]. \quad (21)$$

In view of the above result, a comment is in place. While the off-diagonal susceptibility provides all the crucial information that reveals the presence of a Berry singularity, i.e., (i) it peaks at the singularities and (ii) its sign is opposite for the two Berry singularity branches, its properties are generally not robust when the system is embedded in a “dirty or noisy” environment. For these reasons  $\chi_{12}(\mathbf{B})$  cannot form the basis for the lock-in technique which I wish to propose in this work. In stark contrast, the definition of BSM in Eq. (20) relies on the presence of the spatiotemporally varying fields  $\mathcal{B}(\mathbf{X})$  which can be employed as the reference signal to convolute the response of the system encoded in  $\mathbf{P}$ , and thus enable experimental protocols which allow filtering out the contributions originating from noise or/and disorder.

It is important to clarify that the construction of the BSM bears, up to some extent, similarities to the topological marker introduced by Bianco and Resta in Ref. 87, and further developed in Refs. 88, 89 and others. The main common feature is that, under a suitable limit, the BSM becomes a topological invariant quantity similar to

the topological marker. However, in stark contrast to the latter, the BSM is aimed at being constructed using experimentally-inferred quantities, while the topological marker is more suitable for predicting the local topological properties of the system from a given Hamiltonian. Another crucial difference is that the BSM provides the charge of the Berry singularities across topological phase transitions, while the topological marker provides the local value of the topological invariant of the system. Finally, an additional distinctive feature is that the BSM constitutes a quantity which probes the spacetime non-locality of the system, since it is evaluated using a particular combination of values of  $\mathcal{A}[\mathcal{B}(\mathbf{X})]$  obtained at different spacetime coordinates  $\mathbf{X}$ .

## VII. BERRY SINGULARITY MARKER AND QUANTUM GEOMETRY

The construction of the BSM relies on the presence of the quantity  $\text{Tr}[\tilde{\chi}(\mathbf{B})]$  whose properties remain to be investigated. As I argued earlier, this trace appears capable of quantifying the distance of the system from a Berry singularity. Indeed, reaching to such a conclusion is justifiable since, at it emerges from previous works [48, 52, 58] and I further clarify here, the susceptibility tensor  $\tilde{\chi}$  relates to the quantum metric tensor  $\check{g}$ .

To demonstrate their precise connection, I re-express the susceptibility tensor through the eigenstates of the Hamiltonian, since these are employed for the construction of the quantum metric. Therefore, in terms of the adiabatic Bloch eigenstates  $|\mathbf{u}_a(\mathbf{K}, \mathbf{B})\rangle$  corresponding to the energy bands  $E_a(\mathbf{K}, \mathbf{B})$ ,  $\tilde{\chi}$  is decomposed into the so-called paramagnetic  $\tilde{\chi}^{(\text{p})}$  and diamagnetic parts  $\tilde{\chi}^{(\text{d})}$ . The former contribution is a result of linear response of the system with vertices defined by the generalized paramagnetic currents for  $\mathcal{B} = 0$ . In an operator form, these currents are determined by the matrix elements:

$$J_n^{ab} = -\langle \mathbf{u}_a | \partial_{B_n} \hat{H} | \mathbf{u}_b \rangle \equiv (E_a - E_b) \langle \mathbf{u}_a | \partial_{B_n} \mathbf{u}_b \rangle, \quad (22)$$

where the argument  $(\mathbf{K}, \mathbf{B})$  is implied in all the above functions. In contrast, the diamagnetic contribution stems from the expectation value of the derivative of the above currents. Straightforward calculations, reveal that the diagonal elements of the paramagnetic part read as:

$$\chi_{nn}^{(\text{p})} = \int_{\text{BZ}} \frac{dk}{2\pi} \sum_a 2 \langle \partial_{B_n} \mathbf{u}_a | (\hat{H} - E_a) | \partial_{B_n} \mathbf{u}_a \rangle n_F(E_a), \quad (23)$$

and their diamagnetic counterparts are obtained as:

$$\chi_{nm}^{(\text{d})} = - \int_{\text{BZ}} \frac{dk}{2\pi} \sum_a \langle \mathbf{u}_a | \partial^2 \hat{H} / \partial B_n^2 | \mathbf{u}_a \rangle n_F(E_a), \quad (24)$$

where I suppressed the various arguments for compactness. In the above,  $n_F(\epsilon)$  defines the Fermi-Dirac distribution for an energy  $\epsilon$ , while the indices  $a, b$  label the

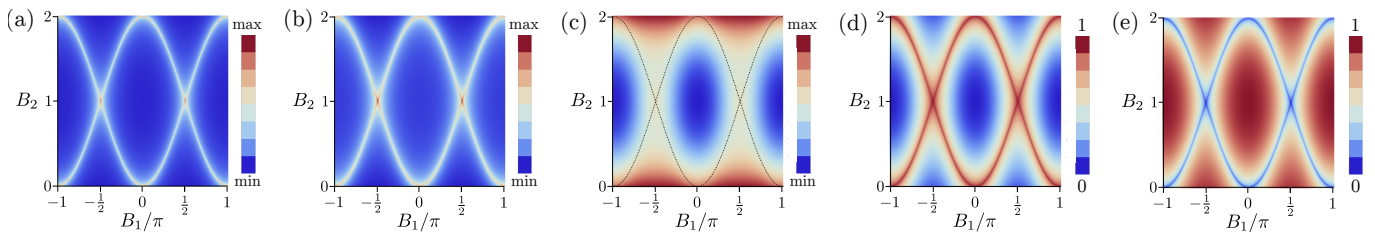


FIG. 4. Numerical results for (a)  $\text{Tr}(\tilde{\chi})$ , (b)  $\text{Tr}(\tilde{\chi}^{(p)})$ , (c)  $\text{Tr}(\tilde{\chi}^{(d)})$ , and (d/e)  $|\text{Tr}(\tilde{\chi}^{(p/d)})|/\sqrt{[\text{Tr}(\tilde{\chi}^{(p)})]^2 + [\text{Tr}(\tilde{\chi}^{(d)})]^2}$ . From panels (a)-(b) one confirms that the paramagnetic/geometric contribution dominates the total susceptibility in the vicinity of the Berry singularity branches. Instead, the diamagnetic component shown in (c) is practically constant along these branches, which are overlaid with dot-dashed lines. Panels (d) and (e) present a comparison between the normalized paramagnetic and diamagnetic contributions, which confirm once again the dominance of the former near Berry singularities. In fact, the paramagnetic/geometric part is constant in almost the entire synthetic space. Deviation from this universal behavior is obtained near the points  $\mathbf{B} = (\pm\pi/2, 1)$  and  $\mathbf{B} = (\pi, 2)$  in which case the Hamiltonian cannot be linearized with respect to neither  $\mathbf{K}$  nor  $\mathbf{B}$ . All the calculations are carried out for  $k_0 = M = 0$ .

Bloch eigenvectors. In the case of the model of Eq. (2), the indices  $a, b$  run over the values  $\pm$ , and the paramagnetic (diamagnetic) susceptibility presented above leads to the contribution of the first (second) row in Eq. 14.

At zero temperature only the occupied band of energy  $E_-(\mathbf{K}, \mathbf{B}) = -|\mathbf{d}(\mathbf{K}, \mathbf{B})|$  contributes to the susceptibility. Hence, the expressions for the susceptibilities simplify further. By employing the projectors  $\hat{P}_a$  of the Bloch states  $|\mathbf{u}_a\rangle$ , one arrives at the following expression for the paramagnetic contribution:

$$\chi_{nn}^{(p)}(\mathbf{B}) = \int_{\text{BZ}} \frac{dk}{2\pi} 4|\mathbf{d}(\mathbf{K}, \mathbf{B})|g_{nn}(\mathbf{K}, \mathbf{B}), \quad (25)$$

where I introduced the diagonal components of the quantum metric tensor of the occupied band

$$g_{nn} = \langle \partial_{B_n} \mathbf{u}_- | (\hat{\mathbb{1}} - \hat{P}_-) | \partial_{B_n} \mathbf{u}_- \rangle, \quad (26)$$

which is in the present situation defined in terms of the synthetic coordinates  $\mathbf{B}$ , instead of the base space coordinates  $\mathbf{K}$ . The above definition of the diagonal quantum metric implies that the quantum distance  $ds$ , is given by the expression  $ds^2 = g_{nm}dB_n dB_m$  with  $n, m = 1, 2$ , where also the similarly-defined off-diagonal components of  $\tilde{\chi}$  are involved. The quantum metric tensor for the occupied band reads as:

$$g_{nn}(\mathbf{K}, \mathbf{B}) = \left[ \frac{1}{2} \hat{\mathbf{d}}(\mathbf{K}, \mathbf{B}) \times \partial_{B_n} \hat{\mathbf{d}}(\mathbf{K}, \mathbf{B}) \right]^2. \quad (27)$$

Remarkably, near a Berry singularity, the emergent “minimal” coupling to the external fields, that reads  $\mathbf{K} \mapsto \mathbf{K} - \mathbf{B}$  or  $\mathbf{K} \mapsto \mathbf{K} + \mathbf{B}$  depending on the location of the Berry singularity, implies that each diagonal element of the quantum metric  $g_{nn}$  becomes approximately equal to the squared modulus of the respective component  $[A_n(\mathbf{K}, \mathbf{B}_s)]^2$  of the Berry vector potential. Note that in the latter I also inserted the dependence of the Berry vector potential on the added external field  $\mathbf{B}$ .

From the above, one concludes that the trace of the quantum metric encodes information regarding the Berry vorticity density, i.e., the integrand of Eq. 5, which blows up when the system is tuned at the Berry singularity. Even more, since near each Berry singularity the Hamiltonian can be linearized with respect to  $\mathbf{K}$ , and concomitantly  $\mathbf{B}$ , the diamagnetic contribution of each Berry singularity to the susceptibility is negligible and, thus, variations of the susceptibility in the vicinity of the Berry singularity branches are mainly dictated by its geometric part. In fact, the geometric contribution  $\text{Tr}[\tilde{\chi}(\mathbf{B}_s)]$  is expected to take the same value at all the positions in  $\mathbf{B}$  space which correspond to Berry singularities. Note, however, that this holds as long as the Hamiltonian is linearizable in terms of both fields  $B_{1,2}$ . If this requirement is not met for some value of  $\mathbf{B}_s$ , the geometric contribution will differ compared to this universal value.

The above properties are confirmable by means of a quantitative exploration of the trace of the total, paramagnetic, and diamagnetic susceptibilities in the case of the model interest. Panels (a)-(c) of Fig. 4 depict the three types of susceptibility traces in the sequence mentioned. One observes that the total susceptibility is mainly determined by its geometric part in the vicinity of the Berry singularity branches, where the diamagnetic part remains practically constant. Panels (d) and (e) present the normalized paramagnetic and diamagnetic contributions. Indeed the geometric part dominates near the Berry singularities. Even more, its heat map features a higher contrast, thus implying that it shows more abrupt variations compared to its diamagnetic analog.

Another important aspect is that the geometric component of the trace takes almost the same value for almost the entire part of the Berry singularity branches, with the only exceptions being the neighborhoods of  $\mathbf{B} = (\pm\pi/2, 1)$  and  $\mathbf{B} = (\pi, 2)$ . The reason is that for these values, the term  $\sin k$  or  $\cos k$  appearing in  $\mathbf{d}(\mathbf{K}, \mathbf{B})$  does not contain a linear term  $\propto k$  in its Taylor expansion about the gap-closing wavenumbers  $k = \{\pm\pi/2, \pi\}$ .

The demonstrated connection between  $\tilde{g}$  and  $\tilde{\chi}$ , sheds

light to the results of the previous section and in particular the limit obtained in Eq. (18). Using the above definitions, the paramagnetic contribution of the latter equation is re-expressed in the following form:

$$\frac{I_s^{(p)}(\mathcal{B} \rightarrow 0)}{\pi} \approx \mathcal{B}^2 \int_{\text{BZ}} \frac{dk}{2\pi} 4|d(\mathbf{K}, \mathbf{B}_s)| \text{Tr}[\hat{g}(\mathbf{K}, \mathbf{B}_s)], \quad (28)$$

which is analogous to the result obtained in Ref. 58 to describe the relation between the power spectrum of fluctuations and the quantum geometry. The possibility of relating response functions to the quantum metric and geometric tensor in general, as well as the connection to the fluctuations dissipation theorem had been already pointed out by Provost and Vallee in their seminal paper [48]. Here, I instead explore the zero-frequency response of the system, since I focus on band touchings.

Notably, the study of the influence of the quantum geometry in static response has recently picked up significant attention in relation to the properties of superfluid density of multiband superconductors harboring flat bands [90, 91]. In the present work, the aim is clearly different, and concerns developing an approach to detect Berry singularities in a disorder-immune fashion.

### VIII. IMPLEMENTATION OF THE BSM USING SPACETIME TEXTURES

The definition of the BSM in Eq. (20) requires the implementation of a closed loop in synthetic space, which can be generated by considering that  $\mathcal{B}$  varies in space and/or time in a periodic fashion. The desired strategy is to consider spatial/spacetime texture profiles for  $\mathcal{B}(\mathbf{X})$ , which can yield a nonzero spacetime vorticity defined as:

$$Q_{\mathcal{B}} = -\frac{1}{2\pi} \oint_{\mathcal{C}_{\mathbf{X}}} d\mathbf{X} \cdot \sum_{n,m} \varepsilon_{nm} \hat{\mathcal{B}}_n(\mathbf{X}) \frac{\partial \hat{\mathcal{B}}_m(\mathbf{X})}{\partial \mathbf{X}} \quad (29)$$

with  $\mathcal{C}_{\mathbf{X}}$  a spacetime loop encircling the vortex contained in the  $\mathcal{B}(\mathbf{X})$  field. Also here, the indices read  $n, m = 1, 2$  since  $\mathbf{X} = (X_1, X_2) = (x, t)$  spans a Euclidean metric space within the semiclassical picture adopted throughout this work. See Fig. 5 for a schematic of possible types of such spacetime vortices.

By exploiting the general connection between the winding number and the vorticity, it is convenient to assume a texture of the form  $\mathcal{B}(\omega) = \mathcal{B}(\cos(\nu\omega), \sin(\nu\omega))$  with  $\omega \in [0, 2\pi)$ , which describes simultaneously a circle  $\mathbb{S}^1$  or a compactifiable line along any direction in 2D spacetime  $\mathbf{X}$ . The above texture gives rise to a nonzero winding number  $w_{\mathcal{B}} = \nu \in \mathbb{Z}$ , which is defined through the expression:

$$w_{\mathcal{B}} = \int_0^{2\pi} \frac{d\omega}{2\pi} \sum_{n,m} \varepsilon_{nm} \hat{\mathcal{B}}_n(\omega) \frac{d\hat{\mathcal{B}}_m(\omega)}{d\omega}. \quad (30)$$

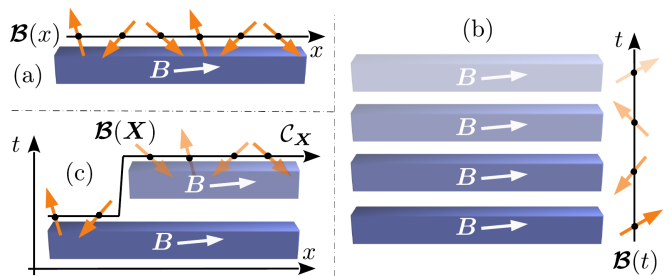


FIG. 5. Three different ways to generate a spacetime texture for the perturbation  $\mathcal{B}(\mathbf{X})$ . One can employ a spiral defined solely in spatial/time coordinates, as shown in (a)/(b), or a spiral unfolding along a spacetime line  $\mathcal{C}_{\mathbf{X}}$ . To ensure that  $\mathcal{C}_{\mathbf{X}}$  is equivalent to a circle  $\mathbb{S}^1$ , the values for  $\mathcal{B}(\mathbf{X})$  are required to be identical at the beginning and end of the path.

With the help of the above, I now write the BSM defined in Eq. (20) as follows:

$$\begin{aligned} Q(\mathcal{B}, \mathcal{B}) &= \int_0^{2\pi} \frac{d\omega}{\pi} \frac{d\hat{\mathcal{B}}(\omega)}{d\omega} \cdot \mathcal{A}[\mathcal{B}, \mathcal{B}(\omega)] \\ &\equiv - \int_0^{2\pi} \frac{d\omega}{\pi} \hat{\mathcal{B}}(\omega) \cdot \frac{d\mathcal{A}[\mathcal{B}, \mathcal{B}(\omega)]}{d\omega}. \end{aligned} \quad (31)$$

Note that it is convenient to normalize the BSM by suitably choosing the spacetime profile of  $\mathcal{B}(\mathbf{X})$  so that  $Q_{\mathcal{B}} = 1$  or  $w_{\mathcal{B}} = 1$ . In the remainder, I solely consider spacetime textures which are characterized by a winding of a single positive unit of spacetime winding/vorticity.

This section concludes with a technical note regarding the construction of the line integral in Eq. (20) and its derivative definitions discussed in this section. Since in the present case there are two branches of Berry singularities in synthetic space, and not isolated points, it is required to avoid the contribution from other singularities along the direction of the line. This can be ensured by considering a discrete implementation of the line integral, in which case, the integral  $\int_0^{2\pi} d\omega/2\pi$  needs to be replaced by the sum  $1/L \sum_n$  where  $n = 1, \dots, L$ , with  $L$  corresponding to the number of points comprising the discrete loop. Considering a discrete loop for the construction of the BSM is the most natural approach, since in experiments the spatial/time resolution of the probe cannot reach zero.

### IX. QUANTITATIVE ANALYSIS OF THE BSM IN THE “CLEAN” CASE

It is straightforward to numerically confirm these conclusions by evaluating the BSM defined in, for instance, Eq. (20) for a texture of the type  $\mathcal{B}(\omega) = \mathcal{B}(\cos \omega, \sin \omega)$  with  $w_{\mathcal{B}} = 1$ . Here,  $\omega \in [0, 2\pi)$  parametrizes the synthetic texture loop. Within the semiclassical limit, the evaluation of the BSM relies on employing the bulk Hamiltonian which is assumed to adiabatically follow

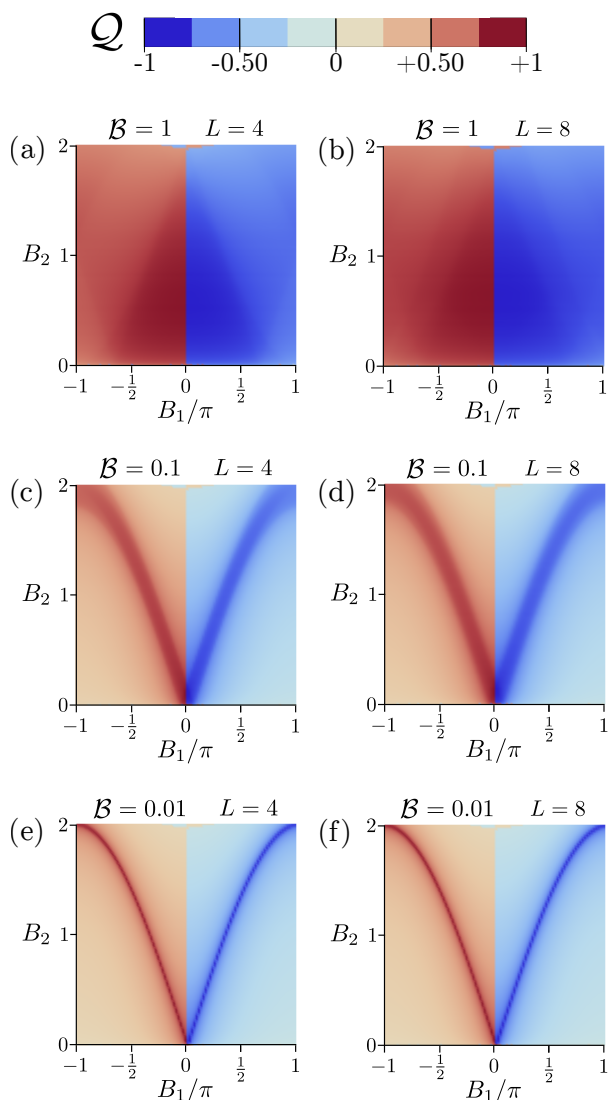


FIG. 6. Numerically evaluated Berry singularity marker (BSM). The panels depict a heat map of the BSM value  $\mathcal{Q}$ , according to the colorcoding presenting on the top of the figure. The parameter window coincides with the one considered in Figs. 1 and 2. Panels {(a), (c), (e)} and {(b), (d), (f)} are calculated for a different period of the synthetic texture imposed on the spatiotemporally varying fields  $\mathcal{B} = \mathcal{B}(\cos \omega, \sin \omega)$ , as this is parametrized by the angle  $\omega \in [0, 2\pi)$ . In the sequences {(a), (c), (e)} and {(b), (d), (f)}, the resolution increases from left to right, according to the three values  $\mathcal{B} = \{1, 0.1, 0.01\}$ . One concludes that enhancing the resolution is crucial to be in a position to discern the Berry singularities through the desired quantization of the BSM. In contrast, increasing the period of the texture, i.e., the sampling points, does not bring drastic improvements to the BSM outcome. Therefore, *in the clean case*, a discrete loop with a few points is sufficient to capture the presence of Berry singularities. In the calculations,  $\text{Tr}(\tilde{\chi}_{\text{BS}})$  was replaced by  $\text{Tr}[\tilde{\chi}(B_1 = \cos^{-1}(B_2 - 1), B_2)]$ , which is the respective value obtained for the nearest Berry singularity to point  $\mathcal{B}$ .

the spatially varying parameters  $\mathcal{B}(\omega)$ . Therefore, within this limit,  $\omega$  plays the role of either a spatial, or a time, or a spacetime coordinate. In this section, I numerically explore the BSM for the model of Eq. (2) with  $k_0 = M = 0$  using the definition contained in the first line of Eq. (31).

The respective numerical results are presented in Fig. 6. In this set of results I have considered the three different values  $\mathcal{B} = \{1, 0.1, 0.01\}$ , which are ordered from left to right according to the increasing resolution of the experimental probe that these represent. In addition, I have assumed a synthetic texture of four and eight sites, i.e.,  $L = \{4, 8\}$ . The numerical results confirm two anticipated trends. First of all, increasing the resolution by decreasing  $\mathcal{B}$  can select out the Berry singularity branches. As seen from the respective panels,  $\mathcal{B}$  essentially determines the width of a strip which encloses the singularity branches. This strip narrows down by reducing  $\mathcal{B}$ . The second expected feature inferred from these results concerns the “sharpening” of the BSM thanks to the increase of the number of sampling points  $L$ . Nonetheless, this improvement ends up to be very small here, thus, revealing that synthetic textures with short lengths  $L$  can already capture the presence of the Berry singularities quite satisfactorily. As is discussed in the next section, this is not the case when disorder is introduced, in which case it is desirable to either increase  $L$  or the number of cycles  $N_c$ , in order to apply the lock-in technique and improve the BSM outcome.

## X. DISORDER AND LOCK-IN TOMOGRAPHY

Up to this point I have discussed and numerically evaluated the BSM in “clean” systems. However, several types of noise and disorder are generally present in the platforms studied in experiments. Therefore, in order to address such a realistic scenario, I here consider the presence of disorder, and demonstrate that the construction of BSM paves the way for disorder-free detection of Berry singularities and, in turn, topological phase transitions.

In the present work, disorder is introduced in the model of Eq. (2) by considering that  $k_0$  and  $M$  are spatiotemporally fluctuating. Within the adiabatic framework adopted here, it is not necessary to specify the origin and characteristics of these fluctuations. The key consequence of disorder here is that, when one evaluates the BSM by considering (for instance) a circular path parametrized by  $\mathcal{B}(\omega) = \mathcal{B}(\cos \omega, \sin \omega)$ ,  $k_0$  and  $M$  are also dependent on  $\omega$ . In the remainder, I consider Anderson-type of disorder, that is, the parameters  $k_0$  and  $M$  take random values in the symmetric intervals  $[-\delta k_0, \delta k_0]$  and  $[-\delta M, \delta M]$ , respectively, with  $\delta k_0$  and  $\delta M$  non-negative. Note that the variations in  $(k_0, M)$  can be effectively absorbed by redefining  $(\mathcal{B}_1, \mathcal{B}_2)$ , as  $(\mathcal{B}_1 + \delta \mathcal{B}_1, \mathcal{B}_2 + \delta \mathcal{B}_2)$ , with  $\delta \mathcal{B}_{1,2} \in \mathbb{R}$ .

It is instructive to first shed light on the effects of weak disorder, i.e., with  $\delta \mathcal{B}_{1,2}$  smaller or comparable to the energy resolution of the experimental probe  $\mathcal{B}$ . In this

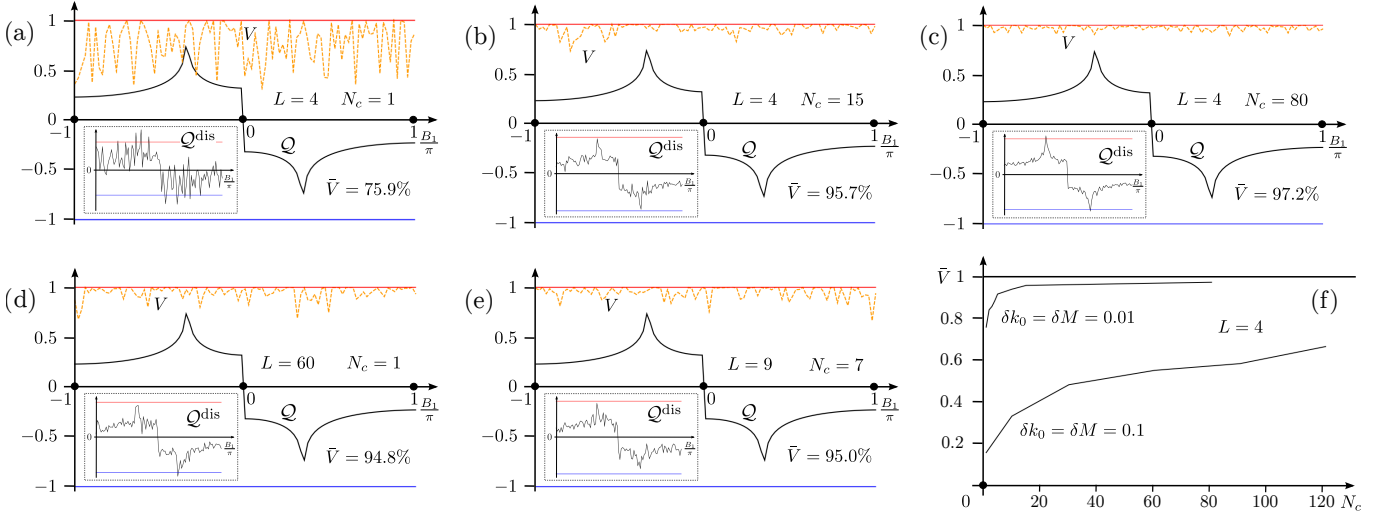


FIG. 7. Numerical investigation of the impact of disorder on the BSM along a cut of Fig. 6 for fixed  $B_2 = 1.5$ . Panels (a)-(c) show the obtained BSM in the absence of disorder ( $Q$ ), the visibility ( $V$ ), the averaged visibility ( $\bar{V}$ ) over the results obtained for the considered  $B_1$  values, and the inset depicts the respective BSM in the presence of disorder ( $Q^{\text{dis}}$ ). In these panels the period of the synthetic texture is the same, but the number of sampling cycles vary. It becomes obvious that the visibility increases with the increase of  $N_c$ . Panels (d) and (e) contain similar results as the previous ones, but with the consideration of alternative strategies in regards to the length of the texture and the sampling cycles. It appears that for comparable number of the total sampling points  $LN_c$ , which are  $\{60, 60, 63\}$  in panels  $\{(b), (d), (e)\}$  of interest, maximizing the number of cycles yields the optimal result. The first five panels discuss random disorder of a strength  $\delta k_0 = \delta M = 0.01$ . Panel (f) shows the averaged visibility obtained for fixed  $L = 4$ , as a function of the number of sampling cycles  $N_c$ , for two different strengths of disorder. The plots were obtained by a connecting isolated points whose values are provided in App. B. One observes that increasing  $N_c$  improves the visibility with, as expected, stronger disorder requiring more cycles to be suppressed. In all the above calculations I used  $\mathcal{B} = 0.001$  and considered a sampling step of 0.01 in terms of  $B_1/\pi$  to reduce the simulations runtime. In contrast, the calculations in Fig. 6 were performed for a step 0.001 which captured the quantization of the peak, which is however missed here. Nonetheless, this does not influence the general conclusions. Finally, note that the red (blue) line corresponds to 1 (-1) also in the inset.

case, the integral  $I_s^{\text{dis}}$  defined as in Eq. (15) but now in the presence of disorder, can be expanded up to linear order in both  $\mathcal{B}_{1,2}$  and  $\delta\mathcal{B}_{1,2}$ , which in the spirit of Eq. (16) here leads to the approximate expression:

$$\frac{I_s^{\text{dis}} - I_s}{I_s} \approx -\frac{1}{\pi} \oint_{\mathcal{C}_{\mathcal{B}_s}} \sum_{n,m} \frac{d\hat{\mathcal{B}}_n \varepsilon_{nm} \chi_{ml}(\mathcal{B}_s)}{\text{Tr}[\hat{\chi}(\mathcal{B}_s)]} \frac{\delta\mathcal{B}_\ell}{\mathcal{B}}, \quad (32)$$

where  $I_s$  defines the contribution for zero disorder and is given by Eq. (16). Besides immediately spoiling the possible quantization of the BSM, the presence of disorder can effectively reduce the resolution and drastically suppress the BSM near the Berry singularities, thus, leading to situation akin to the ones shown in Fig. 6(a) and (b).

In order to remedy these issues, I here propose to employ an experimental protocol which follows the principle of the lock-in amplifier [73]. This principle is a mere consequence of the orthogonality of sinusoidal functions. The potential applicability of this principle becomes apparent in the present situation after considering a circular path for the loop  $\mathcal{C}_{\mathcal{B}}$ . For this case, the last term of Eq. (32) retains contributions of the form:  $\int_0^{2\pi} d\omega \{\cos \omega, \sin \omega\} \delta\mathcal{B}_{1,2}(\omega)$ . When the variations  $\delta\mathcal{B}_{1,2}(\omega)$  are either completely independent of  $\omega$ , or, if

they can be expanded in a Fourier series consisting of terms containing higher harmonics of  $\omega$ , the above contributions drop out. In any other situation, disorder needs to be fully accounted for when calculating the BSM. This problem constitutes a typical issue in signal processing when noise is present. There, the contribution of disorder becomes decoupled by considering a sufficiently large number  $N_c$  of sampling cycles, so that the integrals average out to zero.

To demonstrate how this lock-in tomography of Berry singularities becomes realized, I first consider the case of weak disorder. I first focus on this regime to infer the optimal strategies that lead to suppression of the contributions of disorder to the BSM. To quantify the impact of disorder on the BSM, I introduce the visibility<sup>2</sup>:

$$V = 1/\sqrt{1 + (1 - Q^{\text{dis}}/Q)^2} \quad (33)$$

which takes values in the range  $[0, 1]$ . The visibility becomes equal to 1 (0) when the value of  $Q^{\text{dis}}$  is (not) equal to its counterpart  $Q$  defined in the absence of disorder.

<sup>2</sup> Other choices for the visibility are not expected to alter the general trends of the results.

To carry out the evaluation of  $V$ , I consider once again a discrete circular path in the synthetic space, which is parametrized by  $\omega = 2\pi n/L$ , with  $n = 1, 2, 3, \dots, L$ , with  $L$  denoting the number of sites of the synthetic texture. With no loss of generality, I restrict to a single cut of the synthetic space, with  $B_2 = 1.5$ . Similar general conclusions can be drawn for values for  $B_2$ . The disorder profile is here generated using a standard random generator, and every result for a given  $B_1$  is averaged over twenty random disorder realizations.

In the first set of numerical results, I study how the visibility becomes enhanced by increasing  $N_c$ . Specifically, I fix the synthetic texture length to the value  $L = 4$  and vary the number of sampling cycles  $N_c$ , i.e., the integration variable  $\omega$  in Eq. (31) is now defined in the interval  $[0, 2\pi N_c)$ . Indeed, from panels (a)-(c) in Fig. 7, one confirms the relatively fast restoration of the visibility since we are in the limit of weak disorder  $\delta k_0 = \delta M = 0.01$ . One also notes, however, that there exist spikes in the dependence on  $B_1$ , and a generally not so smooth evolution. This is a result of the random disorder considered here. Hence, one should mainly focus on the general trend rather than exact evolution of the profile. In another batch of results, which are presented in Fig. 7(f) I plot the averaged visibility obtained for  $L = 4$  and various values of  $N_c$ . At this point it is natural to ask which approach is preferred for the same number of total sampling points. That is, assuming that the product  $LN_c$  is fixed, what is the optimal ratio between  $L$  and  $N_c$  which suppresses noise faster, i.e., for the smallest possible product  $LN_c$ . An exploration of this sort is presented in panels (d) and (e) of Fig. 7. By comparing the results of panels (b), (d) and (e) it emerges that the optimal strategy is to maximize  $N_c$ . Nevertheless, further investigation is required to reach to generic conclusions.

There is no obvious reason not to expect that the general trends obtained in the weak disorder limit discussed above, do not carry over to the moderate or strong disorder case, in which situation the approximate form in Eq. (32) does not apply any longer. In panel Fig. 7(e) I also present results which address the case of stronger disorder with  $\delta k_0 = \delta M = 0.1$ . Indeed, it becomes clear that similar trends hold also in the present scenario, but the number of cycles  $N_c$  required to suppress the effects of disorder is, without surprise, significantly larger. Additional details regarding the calculations in this limit are provided in App. B. There, I provide further details on the precise results and methods I used to obtain Fig. 7(e).

## XI. CONCLUSIONS AND OUTLOOK

In this work, I introduce an alternative experimental method to characterize topological phase transitions in insulators, which relies on detecting the Berry singularities of the system. The latter are defined in a synthetic space  $\mathbf{K} = (\mathbf{k}, M)$ , spanned by the wave vector  $\mathbf{k}$  labelling the Bloch bands, and a parameter  $M$  which con-

trols the bulk energy gap. Here, I introduce a quantity coined Berry singularity marker (BSM), which signals the detection of a Berry singularity. To evaluate the BSM, one relies on studying the response of the system in the presence of a set of suitable external fields  $\mathbf{F}$ , which enable variations in all components of  $\mathbf{K}$ , and perform a mapping of the Berry singularities to the synthetic space they span. As I show, the BSM becomes sizeable only in the vicinity of Berry singularities, and its value is mainly determined by the susceptibility tensor elements  $\chi_{11,22,12}(\mathbf{B})$ . The off-diagonal susceptibility element determines the sign of the Berry singularity charge, while the trace of the diagonal susceptibility elements provide a notion of distance from the Berry singularity and is in fact related to the trace of the quantum metric [48].

Although previous works [51–57] have highlighted the value of the quantum metric to detect phase transitions, these had not focused on the information which becomes accessed with respect to the Berry singularities. The construction of the BSM that I present here provides a physical quantity which behaves similar to the Berry charge density and, in fact, tends to the topological charge of the Berry singularity it detects. Even more, the BSM further accounts for the sign of the Berry singularity which also yields information regarding the sign of the variation of the topological invariant characterizing the bulk system, and not only its critical line. However, the most remarkable feature of the BSM, is that it can be implemented using spacetime textures of the external fields, which are in this case decomposed as  $\mathbf{F} = \mathbf{B} + \mathcal{B}(\mathbf{X})$ . The constant offsets  $\mathbf{B}$  allow identifying the locations of the Berry singularities in the original  $\mathbf{K}$  space, while the varying part  $\mathcal{B}(\mathbf{X})$  encodes the spacetime synthetic texture. These, in turn, enable the lock-in evaluation of the BSM, therefore providing a unique path towards the noise-free experimental detection of topological phase transitions.

To demonstrate the above properties, in this work I employ a representative AIII topological insulator model, which shares similarities to the celebrated Su-Schrieffer-Heeger (SSH) model [74]. Besides the explicit construction of the BSM in this case, I further carry out a numerical investigation of the BSM in the absence and presence of disorder. In the former case, I study the behaviour of the BSM when various parameters are changed, such as the resolution of the experimental probe, which is represented by the amplitude of the synthetic texture  $\mathcal{B}(\mathbf{X})$ . In connection to disorder, I consider various realizations of weak and moderate strengths of random disorder which effectively modify  $\mathcal{B}(\mathbf{X})$ . My numerical investigations provided evidence for the success of the approach in suppressing the influence of noise/disorder on the evaluation of the BSM. Similar to the principle of the lock-in amplifier, also here the full suppression of disorder is in principle possible by accordingly increasing the number of sampling points. Despite the fact that in a real experiment this approach may face limitations, the present method yet brings forward the BSM as a quantity which encodes all the information regarding the topolo-

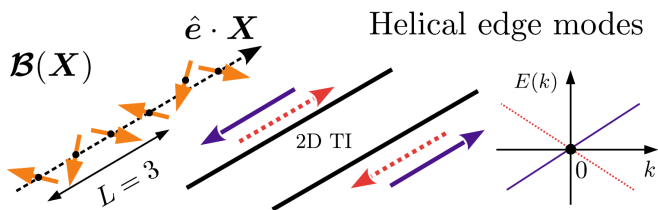


FIG. 8. Experimental setup for benchmarking the theory of Berry singularity markers proposed here. The helical modes on a given edge of a 2D topological insulator can be viewed as a robust Berry singularity, which is protected by time-reversal symmetry. I propose to verify the topological nature of the crossing by evaluating the BSM in the presence of a spiralling magnetic field. Carrying out this experiment in a known 2D topological insulator, such as HgTe quantum wells [92], in the additional presence of intrinsic or controllable disorder, can provide a testbed for the implementation of the BSM method.

gical phase transition, and can be rendered immune to noise and disorder in a straightforward and generic way.

The analysis which I present in this work appears directly testable in two types of currently-accessible experiments. First of all, when  $k_0 = M = 0$  and  $\tau$  corresponds to spin, the model in Eq. (2) effectively describes the gapless helical edge modes which appear on a given edge of a 2D topological insulator [28, 29], such as HgTe quantum wells [92]. See Fig. 8 for a schematic. Notably, this Hamiltonian corresponds to a situation where the system is exactly tuned to a Berry singularity, i.e., which corresponds to the bulk-topology protected crossing point of the two spin-filtered counter-propagating modes [93, 94]. Therefore, to benchmark the present method, one can experimentally infer the BSM by studying the magnetic response of the system to a Zeeman or exchange field which forms a spacetime texture. The spiralling magnetic field is required to wind in a spin plane which involves the direction determined by the polarization of the helical edge modes. Another possible system for the investigation of the BSM approach concerns noisy topo-electric circuits. In fact, the SSH-type of model discussed in Eq. (2) has already been implemented and studied in experiments [95].

One can envisage natural extensions in higher dimensions, where one can in principle follow the very same thinking and construct BSMs based on the response functions of the systems  $\mathbf{P}(\mathbf{X})$ . From Eq. (31) one observes that the BSM can be re-written in terms of derivatives of the conjugate fields, which is closer to the usual construction of the winding number using the  $\mathbf{d}$ -vector of the Hamiltonian. Therefore, suitable antisymmetrized derivatives of  $\mathbf{P}$  with respect to  $\mathbf{B}(\mathbf{X})$  appear promising to lead the construction of the BSM in higher-dimensional systems where the Bloch functions support a winding or a Chern number. Special attention has to be paid, however, when it comes to superconducting systems in classes BDI, D, DIII, since the charge-conjugation symmetry present does not allow to mix functions of a different parity as it was possible here. In a separate

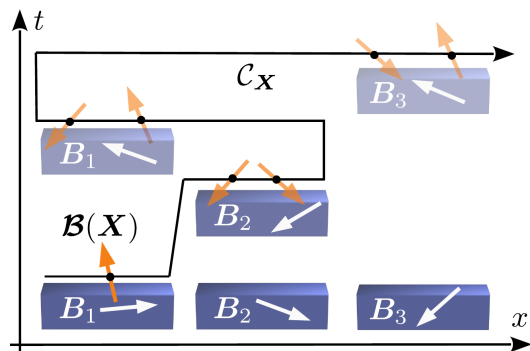


FIG. 9. Sketch for a spacetime texture constructed using multiple systems which are expected to be in principle identical. The degree of topological similarity of the ensemble can be quantified by constructing the ensemble BSM. Possible detunings among the parameter values of the systems of the ensemble function as disorder which can be imprinted in the outcome of the ensemble BSM. Hence, the ensemble BSM in this case provides a measure of collective topological coherence, which can be useful for scaling up devices targetted for quantum computing and other applications. Finally, note that I only placed the three systems along a single axis for simplicity. In general,  $\mathcal{C}_X$  can be any closed loop in quasi-3D or 4D spacetime.

work [96] I propose constructions of BSMs which circumvent this obstacle.

Concluding this work, I remark that the construction of the BSM implies that its applicability goes beyond the characterization of only a single system. Indeed the spatial coordinates of  $\mathbf{X}$  which enter in the evaluation of the BSM may correspond to the locations of completely disconnected systems which are expected to be described by the same Hamiltonian. See for instance Fig. 9 for the depiction of such a spacetime loop. One expects that when the  $\mathbf{B}$  components are tuned to be equal for all the systems involved, and in the absence of disorder, the result of the ensemble BSM will provide a measure of the collective topological coherence. Such a measure appears particularly useful in the process of scaling-up topological systems in order to use them for applications such as universal quantum computing. Therefore, employing the BSM using spacetime textures involving the various components of the device can provide a measure for the topological functionality of the ensemble.

## ACKNOWLEDGEMENTS

I am thankful to Kun Bu and Tilen Čadež for helpful and inspiring discussions which motivated part of the ideas presented in this work. Kun Bu is also acknowledged for his valuable comments on an early version of this manuscript. Finally, I acknowledge funding from the National Natural Science Foundation of China (Grant No. 12074392 and No. 12050410262).

### Appendix A: Alternative coupling to the fields

The presentation and numerical analysis of the main text have been both based on the specific type of coupling of the system to the external field discussed in Sec. III. However, as I already remarked in Sec. III, the choice of couplings is not unique, and this varies depending on the system of interest. It is in fact possible that in several experimental situations engineering the coupling considered in Sec. III may be proven hard to achieve. To tackle such potential shortcomings, in this paragraph I investigate an alternative possibility. Specifically, I consider the situation where the external fields enter the Hamiltonian by shifting the isospin vector  $\mathbf{d}(\mathbf{K})$ , i.e.,  $\mathbf{d}(\mathbf{K}) \mapsto \mathbf{d}(\mathbf{K}) - \mathbf{F}(\mathbf{X})$ . In this case, the energy dispersions of the system become modified according to  $E_{\pm}[\mathbf{K}, \mathbf{F}(\mathbf{X})] = \pm|\mathbf{d}(\mathbf{K}) - \mathbf{F}(\mathbf{X})|$ .

In order to predict the fate of the BSM in the present case, I now proceed by examining the modifications introduced to the Berry singularity branches in synthetic space, as well as to the response of the system, due to the updated coupling to the external fields. With the new coupling, and  $\mathbf{B} = 0$ , the Berry singularities are now given by simultaneously satisfying the gap-closing conditions  $\sin k = B_1$  and  $1 - \cos k + M = B_2$ . As a consequence, the positions of the Berry singularities in the synthetic  $\mathbf{B}$  space are given by the geometric locus:

$$B_1^2 + (B_2 - M - 1)^2 = 1 \quad (\text{A1})$$

which corresponds to a circle centered at the synthetic space point  $\mathbf{B} = (0, M + 1)$ . The locus of Berry singularities is shown in Fig. 10(a), and is superimposed on a heat map depicting the topological invariant of the system obtained as a function of  $(B_1, B_2)$ . Direct calculation of the winding number for  $M = 0$ , yields that the topologically-nontrivial phase with  $w = 1$  appears at the disc enclosed by the Berry singularity circle.

As a next step, I investigate the response of the system to the external fields. Once again, by considering the zero-temperature limit, one finds that the conjugate vector field  $\mathbf{P}[\mathbf{F}(\mathbf{X})]$  now reads as:

$$\mathbf{P}[\mathbf{F}(\mathbf{X})] = - \int_{\text{BZ}} \frac{dk}{2\pi} \frac{\mathbf{d}(\mathbf{K}) - \mathbf{F}(\mathbf{X})}{|\mathbf{d}(\mathbf{K}) - \mathbf{F}(\mathbf{X})|}. \quad (\text{A2})$$

The conjugate fields as functions of  $(B_1, B_2)$  are shown in panels (c) and (e) of Fig. 10, and bear similarities to their counterparts in panels (a) and (c) of Fig. 2, which are obtained for the initial type of coupling. One confirms that the corresponding conjugate field components share the same type of symmetries under mirror operations about the high-symmetry lines. However, they still present a difference, that is, in the present coupling the conjugate fields do not present any periodicity with respect to  $B_1$ .

The susceptibilities are also obtained in a fashion analogous to the one discussed in Sec. V. The related outcomes are shown in panels (b), (d) and (f) of Fig. 10. Leaving aside the lack of periodicity in terms of  $B_1$ , the

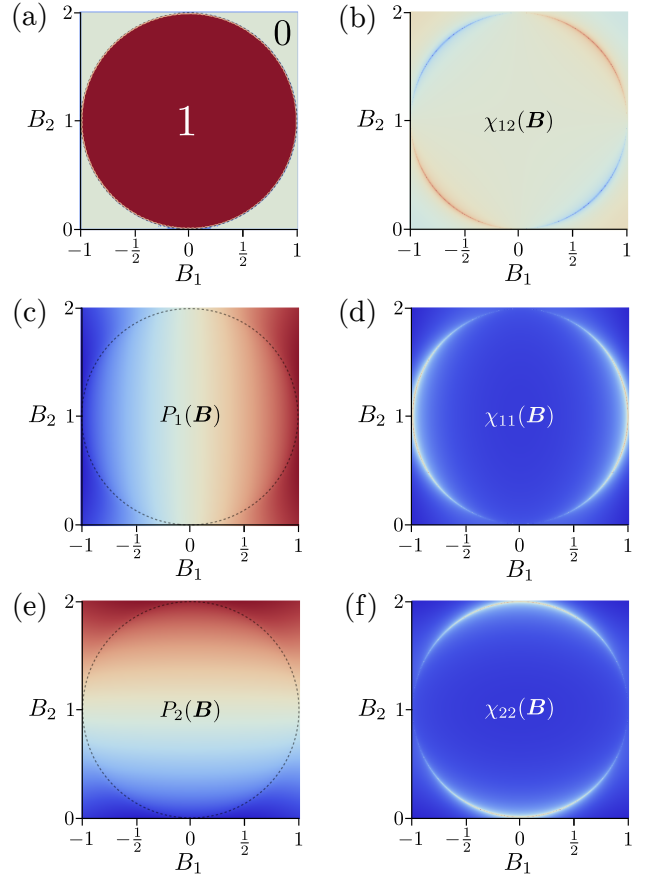


FIG. 10. Properties of the AIII topological insulator with the alternative coupling  $\mathbf{d}(\mathbf{K}) \mapsto \mathbf{d}(\mathbf{K}) - \mathbf{F}(\mathbf{X})$  to the external fields  $\mathbf{F}(\mathbf{X})$ . (a) Topological phase diagram and Berry singularity branches (dot-dashed lines) defined in the synthetic space  $\mathbf{B}$ . Panels (b) and (c) depict the numerically evaluated conjugate fields  $\mathbf{P}(\mathbf{B})$ , while panels (d)-(f) depict the numerically evaluated susceptibility tensor elements  $\chi_{11,22,12}(\mathbf{B})$ . In (b)-(f) the colorcoding varies continuously between deep red to deep blue (■), thus continuously varying from the maximum to the minimum of the depicted function, respectively. Besides the lack of periodicity in terms of  $B_1$ , the obtained results are very similar to the ones of Figs. 2 and 3.

here-found susceptibilities present a similar symmetry behaviour with their counterparts discussed in Sec. V. Most importantly, however, in the present case the diamagnetic contribution to the susceptibility is exactly zero, thus implying that the susceptibility is solely governed by the quantum metric.

Based on the above results, one infers that the construction and behaviour of the BSM for the present type of coupling is expected to be qualitatively similar to the one extensively discussed in this manuscript. For this reason I do not investigate further details of this model.

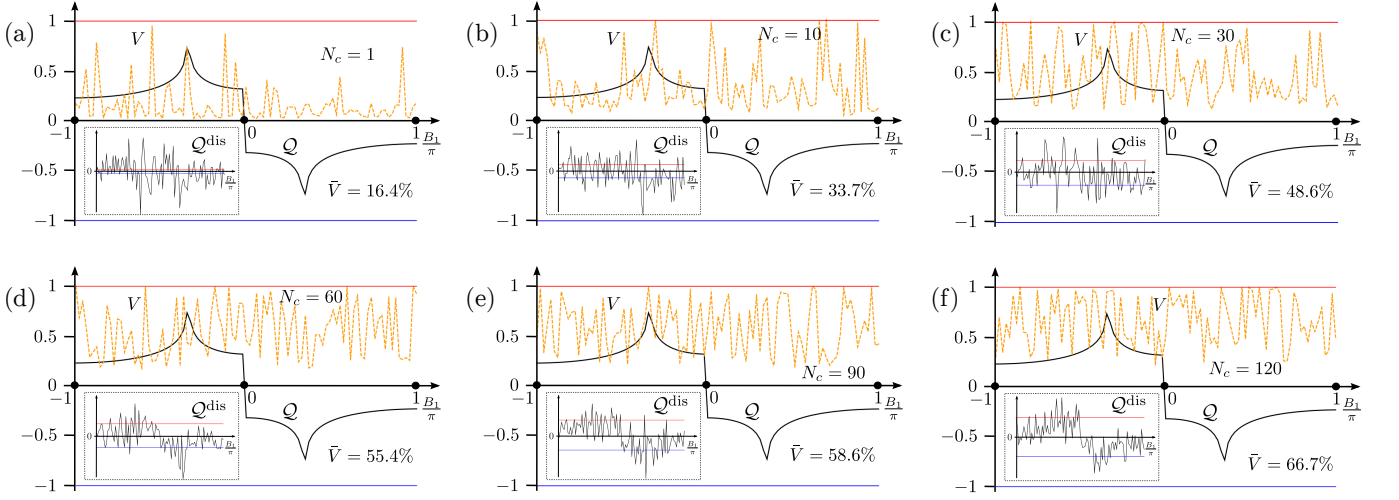


FIG. 11. Numerical investigation of the impact of disorder on the BSM along a cut of Fig. 6 for fixed  $B_2 = 1.5$  and  $\delta k_0 = \delta M = 0.1$ . Panels (a)-(f) show the obtained BSM in the absence of disorder ( $Q$ ), the visibility ( $V$ ), the averaged visibility ( $\bar{V}$ ) over the results obtained for various  $B_1$  values, and the inset depicts the respective BSM in the presence of disorder ( $Q^{\text{dis}}$ ). In these panels the period of the synthetic texture is the same, but the number of sampling cycles vary. It becomes obvious that the visibility increases with the increase of  $N_c$  but this requires more cycles compared to the case of weaker disorder as confirmed by Fig. 7(e). In all the above calculations I used  $\mathcal{B} = 0.001$  and considered a sampling step of 0.01 in terms of  $B_1/\pi$  to reduce the simulations runtime. Finally, note that the red (blue) line corresponds to 1 (-1) also in the inset.

## Appendix B: Additional results regarding disorder

In this appendix, I provide further details regarding the way I constructed Fig. 7(e). For a disorder strength equal to  $\delta k_0 = \delta M = 0.01$ , I performed numerical investigations which provided the following results for  $(N_c, \bar{V}(\%))$ :

(1, 75.9%), (2, 84.1%), (3, 85.7%), (4, 88.4%), (5, 91.6%), (10, 93.9%), (15, 95.7%), and (80, 97.2%). The resulting plot was obtained by simply connecting the above points. A similar approach was followed for the plot in the stronger disorder case, using the results in Fig. 11.

- 
- [1] J. Chen, B. Woods, P. Yu, M. Hoeschele, D. Car, S. Plissard, E. Bakkers, T. Stanescu, and S. Frolov, *Ubiquitous non-Majorana Zero-Bias Conductance Peaks in Nanowire Devices*, Phys. Rev. Lett. **123**, 107703 (2019).
  - [2] P. Yu, J. Chen, M. Gomanko, G. Badawy, E. P. A. M. Bakkers, K. Zuo, V. Mourik, and S. M. Frolov, *Non-Majorana states yield nearly quantized conductance in proximitized nanowires*, Nat. Phys. (2021). <https://doi.org/10.1038/s41567-020-01107-w>.
  - [3] M. Valentini, F. Peñaranda, A. Hofmann, M. Brauns, R. Hauschild, P. Krogstrup, P. San-Jose, E. Prada, R. Aguado, G. Katsaros, *Nontopological zero-bias peaks in full-shell nanowires induced by flux tunable Andreev states*, Science **373**, 82 (2021).
  - [4] H. Zhang, M. W. A. de Moor, J. D. S. Bommer, Di Xu, G. Wang, N. van Loo, C.-X. Liu, S. Gazibegovic, J. A. Logan, D. Car, R. L. M. Op het Veld, P. J. van Veldhoven, S. Koelling, M. A. Verheijen, M. Pendharkar, D. J. Pennachio, B. Shojaei, J. Sue Lee, C. J. Palmström, E. P. A. M. Bakkers, S. Das Sarma, and L. P. Kouwenhoven, *Large zero-bias peaks in InSb-Al hybrid semiconductor-superconductor nanowire devices*, arXiv:2101.11456 (2021).
  - [5] C.-X. Liu, J. D. Sau, T. D. Stanescu, and S. Das Sarma, *Andreev bound states versus majorana bound states in quantum dot-nanowire-superconductor hybrid structures: Trivial versus topological zero-bias conductance peaks*, Phys. Rev. B **96**, 075161 (2017).
  - [6] M. Hell, K. Flensberg, and M. Leijnse, *Distinguishing Majorana bound states from localized Andreev bound states by interferometry*, Phys. Rev. B **97**, 161401(R) (2018).
  - [7] C. Moore, T. D. Stanescu, and S. Tewari, *Two-terminal charge tunneling: Disentangling majorana zero modes from partially separated andreev bound states in semiconductor-superconductor heterostructures*, Phys. Rev. B **97**, 165302 (2018).
  - [8] C.-X. Liu, J. D. Sau, and S. Das Sarma, *Distinguishing topological Majorana bound states from trivial Andreev bound states: Proposed tests through differential tunneling conductance spectroscopy*, Phys. Rev. B **97**, 214502 (2018).
  - [9] C. Reeg, O. Dmytruk, D. Chevallier, D. Loss, and J. Klinovaja, *Zero-energy andreev bound states from quantum dots in proximitized rashba nanowires*, Phys. Rev. B **98**, 245407 (2018).

- [10] B. D. Woods, J. Chen, S. M. Frolov, and T. D. Stanescu, *Zero-energy pinning of topologically trivial bound states in multiband semiconductor-superconductor nanowires*, Phys. Rev. B **100**, 125407 (2019).
- [11] A. Vuik, B. Nijholt, A. R. Akhmerov, and M. Wimmer, *Reproducing topological properties with quasi-Majorana states*, SciPost Phys. **7**, 061 (2019).
- [12] H. Pan and S. Das Sarma, *Physical mechanisms for zero-bias conductance peaks in Majorana nanowires*, Phys. Rev. Research **2**, 013377 (2020).
- [13] E. Prada, P. San-Jose, M. W. A. de Moor, A. Geresdi, E. J. H. Lee, J. Klinovaja, D. Loss, J. Nygård, R. Aguado, and L. P. Kouwenhoven, *From Andreev to Majorana bound states in hybrid superconductor-semiconductor nanowires*, Nat. Rev. Phys. **2**, 575 (2020).
- [14] P. W. Brouwer, M. Duckheim, A. Romito, and F. von Oppen, *Topological superconducting phases in disordered quantum wires with strong spin-orbit coupling*, Phys. Rev. B **84**, 144526 (2011).
- [15] A. R. Akhmerov, J. P. Dahlhaus, F. Hassler, M. Wimmer, and C. W. J. Beenakker, *Quantized Conductance at the Majorana Phase Transition in a Disordered Superconducting Wire*, Phys. Rev. Lett. **106**, 057001 (2011).
- [16] J. Liu, A. C. Potter, K. T. Law, and P. A. Lee, *Zero-bias peaks in the tunneling conductance of spin-orbit-coupled superconducting wires with and without Majorana end-states*, Phys. Rev. Lett. **109**, 267002 (2012).
- [17] D. Bagrets and A. Altland, *Class D spectral peak in majorana quantum wires*, Phys. Rev. Lett. **109**, 227005 (2012).
- [18] E. Prada, P. San-Jose, and R. Aguado, *Transport spectroscopy of NS nanowire junctions with Majorana fermions*, Phys. Rev. B **86**, 180503(R) (2012).
- [19] D. I. Pikulin, J. P. Dahlhaus, M. Wimmer, H. Schomerus, and C. W. J. Beenakker, *A zero-voltage conductance peak from weak antilocalization in a Majorana nanowire*, New J. Phys. **14**, 125011 (2012).
- [20] D. Roy, N. Bondyopadhyaya, and S. Tewari, *Topologically trivial zero-bias conductance peak in semiconductor Majorana wires from boundary effects*, Phys. Rev. B **88**, 020502(R) (2013).
- [21] J. D. Sau and S. Das Sarma, *Density of states of disordered topological superconductor-semiconductor hybrid nanowires*, Phys. Rev. B **88**, 064506 (2013).
- [22] F. Domínguez, J. Cayao, P. San-Jose, R. Aguado, A. L. Yeyati, and E. Prada, *Zero-energy pinning from interactions in Majorana nanowires*, npj Quantum Mater. **2**, 13 (2017).
- [23] A. Altland and M. R. Zirnbauer, *Nonstandard Symmetry Classes in Mesoscopic Normal-Superconducting Hybrid Structures*, Phys. Rev. B **55**, 1142 (1997).
- [24] A. P. Schnyder, S. Ryu, A. Furusaki, and A. W. W. Ludwig, *Classification of topological insulators and superconductors in three spatial dimensions*, Phys. Rev. B **78**, 195125 (2008).
- [25] A. Kitaev, *Periodic table for topological insulators and superconductors*, AIP Conf. Proc. **1134**, 22 (2009).
- [26] S. Ryu, A. P. Schnyder, A. Furusaki and A. W. W. Ludwig, *Topological Insulators and Superconductors: Ten-Fold Way and Dimensional Hierarchy*, New J. Phys. **12**, 065010 (2010).
- [27] J. C. Y. Teo and C. L. Kane, *Topological Defects and Gapless Modes in Insulators and Superconductors*, Phys. Rev. B **82**, 115120 (2010).
- [28] M. Z. Hasan and C. L. Kane, *Colloquium: Topological Insulators*, Rev. Mod. Phys. **82**, 3045 (2010).
- [29] X.-L. Qi and S.-C. Zhang, *Topological Insulators and Superconductors*, Rev. Mod. Phys. **83**, 1057 (2011).
- [30] T. Ö. Rosdahl, A. Vuik, M. Kjaergaard, and A. R. Akhmerov, *Andreev rectifier: A nonlocal conductance signature of topological phase transitions*, Phys. Rev. B **97**, 045421 (2018).
- [31] J. Danon, A. B. Hellenes, E. B. Hansen, L. Casparis, A. P. Higginbotham, and K. Flensberg, *Nonlocal conductance spectroscopy of andreev bound states: Symmetry relations and BCS charges*, Phys. Rev. Lett. **124**, 036801 (2020).
- [32] G. C. Ménard, G. L. R. Anselmetti, E. A. Martinez, D. Puglia, F. K. Malinowski, J. S. Lee, S. Choi, M. Pendharkar, C. J. Palmstrøm, K. Flensberg, C. M. Marcus, L. Casparis, A. P. Higginbotham, *Conductance-matrix symmetries of a three-terminal hybrid device*, Phys. Rev. Lett. **124**, 036802 (2020).
- [33] H. Pan, J. D. Sau, and S. D. Sarma, *Three-terminal non-local conductance in Majorana nanowires: Distinguishing topological and trivial in realistic systems with disorder and inhomogeneous potential*, Phys. Rev. B **103**, 014513 (2021).
- [34] D. I. Pikulin, B. van Heck, T. Karzig, E. A. Martinez, B. Nijholt, T. Laeven, G. W. Winkler, J. D. Watson, S. Heedt, M. Temurhan, V. Svidenko, R. M. Lutchyn, M. Thomas, G. de Lange, L. Casparis, and C. Nayak, *Protocol to identify a topological superconducting phase in a three-terminal device*, arXiv:2103.12217.
- [35] L. S. Ricco, V. K. Kozin, A. C. Seridonio, and I. A. Shelykh, *Accessing the degree of Majorana nonlocality with photons*, arXiv:2105.05925.
- [36] C. J. Bolech and E. Demler, *Observing Majorana bound States in p-Wave Superconductors Using Noise Measurements in Tunneling Experiments*, Phys. Rev. Lett. **98**, 237002 (2007).
- [37] G. Strübi, W. Belzig, M.-S. Choi, and C. Bruder, *Interferometric and Noise Signatures of Majorana Fermion Edge States in Transport Experiments*, Phys. Rev. Lett. **107**, 136403 (2011).
- [38] T. Jonckheere, J. Rech, A. Zazunov, R. Egger, A. Levy Yeyati, and T. Martin, *Giant Shot Noise from Majorana Zero Modes in Topological Trijunctions*, Phys. Rev. Lett. **122**, 097003 (2019).
- [39] J. Manousakis, C. Wille, A. Altland, R. Egger, K. Flensberg, and F. Hassler, *Weak Measurement Protocols for Majorana Bound State Identification*, Phys. Rev. Lett. **124**, 096801 (2020).
- [40] C. W. J. Beenakker and D. O. Oriekhov, *Shot noise distinguishes Majorana fermions from vortices injected in the edge mode of a chiral p-wave superconductor*, SciPost Phys. **9**, 080 (2020).
- [41] V. Perrin, M. Civelli, and P. Simon, *Identifying Majorana bound states by tunneling shot-noise tomography*, Phys. Rev. B **104**, L121406 (2021).
- [42] J. D. Pakizer and A. Matos-Abiague, *Signatures of topological transitions in the spin susceptibility of Josephson junctions*, Phys. Rev. B **104**, L100506 (2021).
- [43] S. Ozaki and M. Ogata, *Universal quantization of the magnetic susceptibility jump at a topological phase transition*, Phys. Rev. Research **3**, 013058 (2021).
- [44] R.-J. Slager, L. Rademaker, J. Zaanen, and L. Balents, *Impurity-bound states and Green's function zeros as local*

- signatures of topology*, Phys. Rev. B **92**, 085126 (2015).
- [45] V. Kaladzhyan and C. Bena, *Obtaining Majorana and other boundary modes from the metamorphosis of impurity-induced states: Exact solutions via the T-matrix*, Phys. Rev. B **100**, 081106(R) (2019).
- [46] N. Sedlmayr, V. Kaladzhyan, and C. Bena, *Analytical and semianalytical tools to determine the topological character of Shiba chains*, Phys. Rev. B **104**, 024508 (2021).
- [47] A. V. Balatsky, I. Vekhter, and J.-X. Zhu, *Impurity-induced states in conventional and unconventional superconductors*, Rev. Mod. Phys. **78**, 373 (2006).
- [48] J. P. Provost and G. Vallee, *Riemannian Structure on Manifolds of Quantum States*, Commun. Math. Phys. **76**, 289 (1980).
- [49] N. Marzari and D. Vanderbilt, *Maximally localized generalized Wannier functions for composite energy bands*, Phys. Rev. B **56**, 12847 (1997).
- [50] I. Souza, T. Wilkens, and R. M. Martin, *Polarization and localization in insulators: Generating function approach*, Phys. Rev. B **62**, 1666 (2000).
- [51] P. Zanardi, H. T. Quan, X. Wang, and C. P. Sun, *Mixed-state fidelity and quantum criticality at finite temperature*, Phys. Rev. A **75**, 032109 (2007).
- [52] P. Zanardi, P. Giorda, and M. Cozzini, *Information-Theoretic Differential Geometry of Quantum Phase Transitions*, Phys. Rev. Lett. **99**, 100603 (2007).
- [53] S. Yang, S.-J. Gu, C.-P. Sun, and H.-Q. Lin, *Fidelity susceptibility and long-range correlation in the Kitaev honeycomb model*, Phys. Rev. A **78**, 012304 (2008).
- [54] Y.-Q. Ma, S. Chen, H. Fan, and W.-M. Liu, *Abelian and Non-Abelian Quantum Geometric Tensor*, Phys. Rev. B **81**, 245129 (2010).
- [55] S. Matsuura and S. Ryu, *Momentum space metric, non-local operator, and topological insulators*, Phys. Rev. B **82**, 245113 (2010).
- [56] Y.-Q. Ma, S.-J. Gu, S. Chen, H. Fan, W.-M. Liu, *The Euler Number of Bloch States Manifold and the Quantum Phases in Gapped Fermionic Systems*, EPL **103**, 10008 (2013).
- [57] F. Piéchon, A. Raoux, J.-N. Fuchs, and G. Montambaux, *Geometric orbital susceptibility: Quantum metric without Berry curvature*, Phys. Rev. B **94**, 134423 (2016).
- [58] T. Neupert, C. Chamon, and C. Mudry, *Measuring the quantum geometry of Bloch bands with current noise*, Phys. Rev. B **87**, 245103 (2013).
- [59] M. Kolodrubetz, V. Gritsev, and A. Polkovnikov *Classifying and measuring geometry of a quantum ground state manifold*, Phys. Rev. B **88**, 064304 (2013).
- [60] M. Kolodrubetz, D. Sels, P. Mehta, and A. Polkovnikov, *Geometry and non-adiabatic response in quantum and classical systems*, Phys. Rep. **697**, 1 (2017).
- [61] T. Ozawa and N. Goldman, *Extracting the quantum metric tensor through periodic driving*, Phys. Rev. B **97**, 201117 (2018).
- [62] D. T. Tran, N. R. Cooper, and N. Goldman, *Quantized Rabi oscillations and circular dichroism in quantum Hall systems*, Phys. Rev. A **97**, 061602 (2018).
- [63] L. Peralta Gavensky, G. Usaj, D. Feinberg, and C. A. Balseiro, *Berry curvature tomography and realization of topological Haldane model in driven three-terminal Josephson junctions*, Phys. Rev. B **97**, 220505(R) (2018).
- [64] R. L. Klees, J. C. Cuevas, W. Belzig, and G. Rastelli, *Many-body Quantum Geometry in Superconductor-Quantum Dot Chains*, Phys. Rev. B **103**, 014516 (2021).
- [65] R. L. Klees, G. Rastelli, J. C. Cuevas, and W. Belzig, *Microwave Spectroscopy Reveals the Quantum Geometric Tensor of Topological Josephson Matter*, Phys. Rev. Lett. **124**, 197002 (2020).
- [66] G. von Gersdorff and W. Chen, *Measurement of Topological Order based on Metric-Curvature Correspondence*, Phys. Rev. B **104**, 195133 (2021).
- [67] P. Roushan, C. Neill, Y. Chen *et al.*, *Observation of topological transitions in interacting quantum circuits*, Nature **515**, 241 (2014).
- [68] M. D. Schroer, M. H. Kolodrubetz, W. F. Kindel, M. Sandberg, J. Gao, M. R. Vissers, D. P. Pappas, A. Polkovnikov, and K. W. Lehnert, *Measuring a topological transition in an artificial Spin-1/2 system*, Phys. Rev. Lett. **113**, 050402 (2014).
- [69] N. Fläschner, B. S. Rem, M. Tarnowski, D. Vogel, D.-S. Lühmann, K. Sengstock, and C. Weitenberg, *Experimental reconstruction of the Berry curvature in a Floquet Bloch band*, Science **352**, 1091 (2016).
- [70] M. Wimmer, H. Price, I. Carusotto, and U. Peschel, *Experimental measurement of the Berry curvature from anomalous transport*, Nat. Phys. **13**, 545 (2017).
- [71] X. Tan, D.-W. Zhang, Q. Liu, G. Xue, H.-F. Yu, Y.-Q. Zhu, H. Yan, S.-L. Zhu, and Y. Yu, *Topological Maxwell Metal Bands in a Superconducting Qutrit*, Phys. Rev. Lett. **120**, 130503 (2018).
- [72] X. Tan, D.-W. Zhang, Z. Yang, J. Chu, Y.-Q. Zhu, D. Li, X. Yang, S. Song, Z. Han, Z. Li, Y. Dong, H.-F. Yu, H. Yan, S.-L. Zhu, and Y. Yu, *Experimental Measurement of the Quantum Metric Tensor and Related Topological Phase Transition with a Superconducting Qubit*, Phys. Rev. Lett. **122**, 210401 (2019).
- [73] W. C. Michels and N. L. Curtis, *A Pentode Lock-In Amplifier of High Frequency Selectivity*, Rev. Sci. Instrum. **12**, 444 (1941).
- [74] W. P. Su, J. R. Schrieffer, and A. J. Heeger, *Solitons in Polyacetylene*, Phys. Rev. Lett. **42**, 1698 (1979).
- [75] R. Jackiw and C. Rebbi, *Solitons with fermion number 1/2*, Phys. Rev. D **13**, 3398 (1976).
- [76] R.-P. Riwar, M. Houzet, J. S. Meyer, and Y. V. Nazarov, *Multi-Terminal Josephson Junctions as Topological Matter*, Nat. Commun. **7**, 11167 (2016).
- [77] E. Eriksson, R.-P. Riwar, M. Houzet, J. S. Meyer, and Y. V. Nazarov, *Topological transconductance quantization in a four-terminal Josephson junction*, Phys. Rev. B **95**, 075417 (2017).
- [78] J. S. Meyer and M. Houzet, *Nontrivial Chern Numbers in Three-Terminal Josephson Junctions*, Phys. Rev. Lett. **119**, 136807 (2017).
- [79] H.-Y. Xie, M. G. Vavilov, and A. Levchenko, *Topological Andreev bands in three-terminal Josephson junctions*, Phys. Rev. B **96**, 161406 (2017).
- [80] H.-Y. Xie, M. G. Vavilov, and A. Levchenko, *Weyl nodes in Andreev spectra of multiterminal Josephson junctions: Chern numbers, conductances, and supercurrents*, Phys. Rev. B **97**, 035443 (2018).
- [81] V. Fatemi, A. R. Akhmerov, and L. Bretheau, *Weyl Josephson Circuits*, Phys. Rev. Research **3**, 013288 (2021).
- [82] L. P. Gavensky, G. Usaj, and C. A. Balseiro, *Topological phase diagram of a three-terminal Josephson junction: From the conventional to the Majorana regime*, Phys. Rev. B **100**, 014514 (2019).

- [83] M. Houzet, J. S. Meyer, *Majorana-Weyl crossings in topological multi-terminal junctions*, Phys. Rev. B **100**, 014521 (2019).
- [84] P. Kotetes, M. T. Mercaldo, and M. Cuoco, *Synthetic Weyl Points and Chiral Anomaly in Majorana Devices with Nonstandard Andreev-Bound-State Spectra*, Phys. Rev. Lett. **123**, 126802 (2019).
- [85] M. T. Mercaldo, P. Kotetes, and M. Cuoco, *Magneto-electrically-Tunable Andreev-Bound-State Spectra and Spin Polarization in P-Wave Josephson Junctions*, Phys. Rev. B **100**, 104519 (2019).
- [86] K. Sakurai, M. T. Mercaldo, S. Kobayashi, A. Yamakage, S. Ikegaya, T. Habe, P. Kotetes, M. Cuoco, and Y. Asano, *Nodal Andreev Spectra in Multi-Majorana Three-Terminal Josephson Junctions*, Phys. Rev. B **101**, 174506 (2020).
- [87] R. Bianco and R. Resta, *Mapping topological order in coordinate space*, Phys. Rev. B **84**, 241106(R) (2011).
- [88] M. D. Caio, G. Möller, N. R. Cooper, and M. J. Bhaseen, *Topological marker currents in Chern insulators*, Nat. Phys. **15**, 257 (2019).
- [89] A. A. Markov and A. N. Rubtsov, *Local marker for interacting topological insulators*, Phys. Rev. B **104**, L081105 (2021).
- [90] S. Peotta and P. Törmä, *Superfluidity in topologically nontrivial flat bands*, Nature Communications **6**, 8944 (2015).
- [91] L. Liang, T. I. Vanhala, S. Peotta, T. Siro, A. Harju, and P. Törmä, *Band geometry, Berry curvature, and superfluid weight*, Phys. Rev. B **95**, 024515 (2017).
- [92] M. König, S. Wiedmann, C. Brüne, A. Roth, H. Buhmann, L. W. Molenkamp, X.-L. Qi, and S.-C. Zhang, *Quantum Spin Hall Insulator State in HgTe Quantum Wells*, Science **318**, 766 (2007).
- [93] C. L. Kane and E. J. Mele, *Quantum Spin Hall Effect in Graphene*, Phys. Rev. Lett. **95**, 226801 (2005).
- [94] C. L. Kane and E. J. Mele, *Z<sub>2</sub> Topological Order and the Quantum Spin Hall Effect*, Phys. Rev. Lett. **95**, 146802 (2005).
- [95] C. H. Lee, S. Imhof, C. Berger, F. Bayer, J. Brehm, L. W. Molenkamp, T. Kiessling, and R. Thomale, *Topoelectrical circuits*, Nat. Commun. **1**, 39 (2018).
- [96] P. Kotetes, *Diagnosing Topological Phase Transitions in 1D Superconductors using Berry Singularity Markers* (tentative title), in preparation.